Combining the Tyrosine Kinase Inhibitor Cabozantinib and the mTORC1/2 Inhibitor Sapanisertib Blocks ERK Pathway Activity and Suppresses Tumor Growth in Renal Cell Carcinoma

Yige Wu[1,2], Siqi Chen[1,2], Xiaolu Yang[1], Kazuhito Sato[1,2], Preet Lal[1], Yuefan Wang[3], Andrew T. Shinkle[1], Michael C. Wendl[1,2,4,5], Tina M. Primeau[1], Yanyan Zhao[1], Alanna Gould[1], Hua Sun[1,2], Jacqueline L. Mudd[1], Jeremy Hoog[1], R. Jay Mashl[1,2], Matthew A. Wyczalkowski[1,2], Chia-Kuei Mo[1,2], Ruiyang Liu[1,2], John M. Herndon[6,7], Sherri R. Davies[1], Di Liu[1], Xi Ding[1], Yvonne A. Evrard[8], Bryan E. Welm[9], David Lum[9], Mei Yee Koh[9], Alana L. Welm[9], Jeffrey H. Chuang[10], Jeffrey A. Moscow[11], Funda Meric-Bernstam[12], Ramaswamy Govindan[1,4], Shunqiang Li[1,4], James Hsieh[1], Ryan C. Fields[4], Kian-Huat Lim[1,4], Cynthia X. Ma[1,4], Hui Zhang[3], Li Ding[1,2,4,6], and Feng Chen[1,4]

ABSTRACT

Current treatment approaches for renal cell carcinoma (RCC) face challenges in achieving durable tumor responses due to tumor heterogeneity and drug resistance. Combination therapies that leverage tumor molecular profiles could offer an avenue for enhancing treatment efficacy and addressing the limitations of current therapies. To identify effective strategies for treating RCC, we selected ten drugs guided by tumor biology to test in six RCC patient-derived xenograft (PDX) models. The multitargeted tyrosine kinase inhibitor (TKI) cabozantinib and mTORC1/2 inhibitor sapanisertib emerged as the most effective drugs, particularly when combined. The combination demonstrated favorable tolerability and inhibited tumor growth or induced tumor regression in all models, including two from patients who experienced treatment failure with FDA-approved TKI and immunotherapy combinations. In cabozantinib-treated samples, imaging analysis revealed a significant reduction in vascular density, and single-nucleus RNA sequencing (snRNA-seq) analysis indicated a decreased proportion of endothelial cells in the tumors. SnRNA-seq data further identified a tumor subpopulation enriched with cell-cycle activity that exhibited heightened sensitivity to the cabozantinib and sapanisertib combination. Conversely, activation of the epithelial–mesenchymal transition pathway, detected at the protein level, was associated with drug resistance in residual tumors following combination treatment. The combination effectively restrained ERK phosphorylation and reduced expression of ERK downstream transcription factors and their target genes implicated in cell-cycle control and apoptosis. This study highlights the potential of the cabozantinib plus sapanisertib combination as a promising treatment approach for patients with RCC, particularly those whose tumors progressed on immune checkpoint inhibitors and other TKIs.

Significance: The molecular-guided therapeutic strategy of combining cabozantinib and sapanisertib restrains ERK activity to effectively suppress growth of renal cell carcinomas, including those unresponsive to immune checkpoint inhibitors.

Introduction

Renal cell carcinoma (RCC) originates from cells in the renal epithelium and accounts for more than 90% of cancers in the kidney (1). Clear cell RCC (ccRCC) is the most common (75%) subtype. In the past 20 years, several targeted immunotherapy agents have been approved by the FDA for the treatment of metastatic RCC, including immune checkpoint inhibitors (ICI), tyrosine kinase inhibitors (TKI), mTOR inhibitors (mTORi), and the anti-VEGF antibody (bevacizumab). Although initially effective for some patients, others display intrinsic resistance (2). Most responders will also eventually acquire resistance (2), necessitating combinational follow-up therapies. In the first-line treatment setting, combinations of two ICIs and ICI plus TKI have shown better outcomes compared with TKI alone for metastatic RCC (3–6). In the second-line treatment setting, patients who have progressed after initial ICI and have not previously received TKI often get single-agent TKI (e.g., cabozantinib) or the lenvatinib plus everolimus combination (3). However, these options may be discontinued due to disease progression or adverse events. Thus, more effective combinational therapies are urgently needed for treating patients with unfavorable prognoses for therapies currently used in the clinic based on biomarkers and prior failed treatments.

[1]Department of Medicine, Washington University in St. Louis, St. Louis, Missouri. [2]McDonnell Genome Institute, Washington University in St. Louis, St. Louis, Missouri. [3]Department of Pathology, Johns Hopkins University, Baltimore, Maryland. [4]Department of Genetics, Washington University in St. Louis, St. Louis, Missouri. [5]McKelvey School of Engineering, Washington University in St. Louis, St. Louis, Missouri. [6]Siteman Cancer Center, Washington University in St. Louis, St. Louis, Missouri. [7]Department of Surgery, Washington University in St. Louis, St. Louis, Missouri. [8]Frederick National Laboratory for Cancer Research, Frederick, Maryland. [9]Huntsman Cancer Institute, University of Utah, Salt Lake City, Utah. [10]The Jackson Laboratory for Genomic Medicine, Farmington, Connecticut. [11]Investigational Drug Branch, National Cancer Institute, Bethesda, Maryland. [12]The University of Texas MD Anderson Cancer Center, Houston, Texas.

Y. Wu, S. Chen, X. Yang, K. Sato, and P. Lal contributed equally to this article.

Corresponding Authors: Li Ding and Feng Chen, Nephrology Division, Washington University in St. Louis, 4523 Clayton Avenue, Box 8126, St. Louis, MO 63110. E-mail: lding@wustl.edu and fchen@wustl.edu

Cancer Res 2023;83:4161–78

doi: 10.1158/0008-5472.CAN-23-0604

Cabozantinib (Cabometyx by Exelixis) is a relatively new receptor tyrosine kinase (RTK) inhibitor approved for first- and second-line treatment for advanced/metastatic RCC. It targets VEGFRs, c-MET, and AXL (7), which are upregulated in many RCC tumor cells due to *VHL* inactivation and are associated with poor prognosis (8–10). Although cabozantinib showed improved survival in clinical trials compared with sunitinib and other drugs (11, 12), resistance eventually developed (7). Besides RTKs, existing data and our own analyses of human RCC specimens (Supplementary Fig. S1A) and a collection of RCC patient-derived xenograft (PDX) models revealed alterations in a number of pathways and factors that may be targeted by treatments, including the mTOR pathway, hypoxia-inducible factor (HIF) pathway, MEK/ERK kinase pathway, angiogenic factors, CDKs, inhibitors of apoptosis (IAP), and histone deacetylases (HDAC).

Sapanisertib (MLN0128, TAK-228, CB228 by Millenium/Takeda/Calithera) is an experimental small-molecule inhibitor of mTOR, targeting both mTOR complexes 1 (mTORC1) and 2 (mTORC2; refs. 13, 14). Although mTOR inhibitors, such as everolimus and temsirolimus, are approved for advanced RCC in the second-line setting, they primarily target mTORC1 rather than mTORC2 and show variable patient responses (15). We hypothesized that newer drugs targeting mTORC1 and mTORC2, such as sapanisertib, might show better efficacy than everolimus by inhibiting the mTOR pathway more completely. A phase I clinical trial (NCT01058707) demonstrated that sapanisertib has a manageable safety profile with preliminary antitumor activity in RCC (16). Furthermore, it has received a fast-track FDA designation for squamous non–small cell lung cancers (17) having *NRF2* mutations or that have previously received chemotherapy and ICIs. Conversely, a recent phase II clinical trial (NCT03097328) showed that sapanisertib alone has minimal efficacy in treatment-refractory metastatic RCC (18). Nonetheless, a sapanisertib plus cabozantinib combination has shown an augmented antitumor effect in mouse hepatocellular carcinoma compared to cabozantinib alone (19), suggesting this combination be investigated for RCC.

Analysis shows that HIF, CDK, IAP, HDAC, and MEK/ERK proteins and related pathways are upregulated in ccRCC tumor tissues (Supplementary Fig. S1; ref. 20). Their inhibition shows some antitumor effects in RCC (21, 22) and other cancers (23, 24). Acriflavine, an FDA-approved HIF1α inhibitor (25), shows efficacy in brain cancer (26). Chromatin remodeling plays a crucial role in RCC oncogenesis (27) and valproic acid (an HDAC inhibitor) has been shown to counteract everolimus (an mTOR inhibitor) resistance in RCC (28). HDAC inhibitors, including panobinostat and β-hydroxybutyrate, may overcome resistance to TKIs. IAP inhibitor birinapant has been investigated in other solid tumors but never in RCC. CDK4/6 inhibitor abemaciclib has been shown to induce RCC PDX tumor regression when combined with sunitinib (21) but has not been investigated with cabozantinib. MEK1 inhibitor selumetinib was shown to enhance the antitumor activity of mTORC1 inhibitor everolimus in RCC (22). Finally, losartan, an angiotensin receptor blocker, modulates the tumor microenvironment, potentially enhancing the effectiveness of other TKIs or targeted therapies in RCC (29). Taken together, evaluating these drugs in RCC PDX models may uncover new therapeutic options for patients with RCC.

On the basis of the rationale described above, we selected ten drugs and tested them on RCC PDX models, ultimately identifying the cabozantinib and sapanisertib combination as the most effective treatment. Mechanistically, this combination inhibits tumor growth by reducing vascular density, blunting MAPK signaling, and downregulating the cell cycle–related targets of E2F transcription factors (TF). It was effective in models derived from tumors resistant to prior antiangiogenic treatment. Our findings suggest that cabozantinib plus sapanisertib could be an effective new treatment option for patients with RCC, even those who failed prior immunotherapy, targeted therapy, and other combinational therapies. Our results show that omics data are valuable in explaining the molecular alterations underlying treatment effects, illustrating resistance mechanisms, and predicting treatment outcomes and the development of potential drug resistance.

Materials and Methods

PDX models and the production of cohorts for drug treatment

All human tissues acquired for experiments were processed in compliance with NIH regulations and institutional guidelines, as approved by the Institutional Review Board at Washington University in St. Louis (WUSTL, St. Louis, MO). Written informed consent forms were obtained from all patients in this study. All animal procedures were approved by the Institutional Animal Care and Use Committee at WUSTL. Immunodeficient NSG mice (NOD.Cg-*Prkdc*^{scid} *Il2rg*^{tm1Wjl}/*SzJ*, Stock No: 005557) were purchased from The Jackson Laboratory. Mice were kept in a temperature-controlled facility on a 12/12-hour light/dark schedule with normal food and water supplies. Six- to 8-week-old female NSG mice were placed under anesthesia and received tumor implantation subcutaneously on both flanks.

Tumor measurement and sample collection

Upon signs of solid tumor establishment, tumor size and body weight were measured twice a week. Tumor volume was measured with calipers and calculated as (mm^3) = length (mm) × width^2 (mm^2) × 0.5 (Supplementary Data S1). When tumors reached a volume of 150–250 mm^3, the mice were assigned into four groups randomly with comparable median and mean tumor volumes. The day of grouping was designated as day 0 of an experiment and was also the first day of treatment. Mice were treated orally with vehicle, single drug, or drug combinations 5 consecutive days a week, and were drug-free on weekends. Cabozantinib was purchased from Selleck (S4001). Sapanisertib was purchased from Sigma (L21907). If tumors reached 2 cm in diameter or there were signs of distress, mice were euthanized, and tumors were collected immediately. Tumors were fixed in 4% paraformaldehyde and snap-frozen in liquid nitrogen for further analyses.

Tumor volumes were evaluated relative to the initial volume (day 0) and expressed as relative tumor volume (RTV). The % tumor growth inhibition (TGI) was calculated as [1 – (mean volume of treated tumors)/(mean volume of control tumors)] × 100%. The significance of tumor inhibition by drug treatment was calculated using unpaired Student *t* tests comparing RTVs between treated and control groups or between combinational therapy and monotherapy groups.

Because of different mortality rates, we adjusted the numbers of mice at the start of treatments to maintain similar numbers within each treatment regimen throughout the treatment period. Specifically, RESL5 and RESL4 models had four mice in each treatment regimen, while RESL3 and RESL12 models had three. For RESL10, the control group had five mice, while the other groups had four mice each. Similarly, for RESL11, the control group had four and the other groups had three each. In **Fig. 1C**, each data point represents the average measurements derived from multiple mice that remained alive at that time point. If a mouse died, the average measurements beyond that time point were calculated solely based on the measurements of the remaining mice within that group.

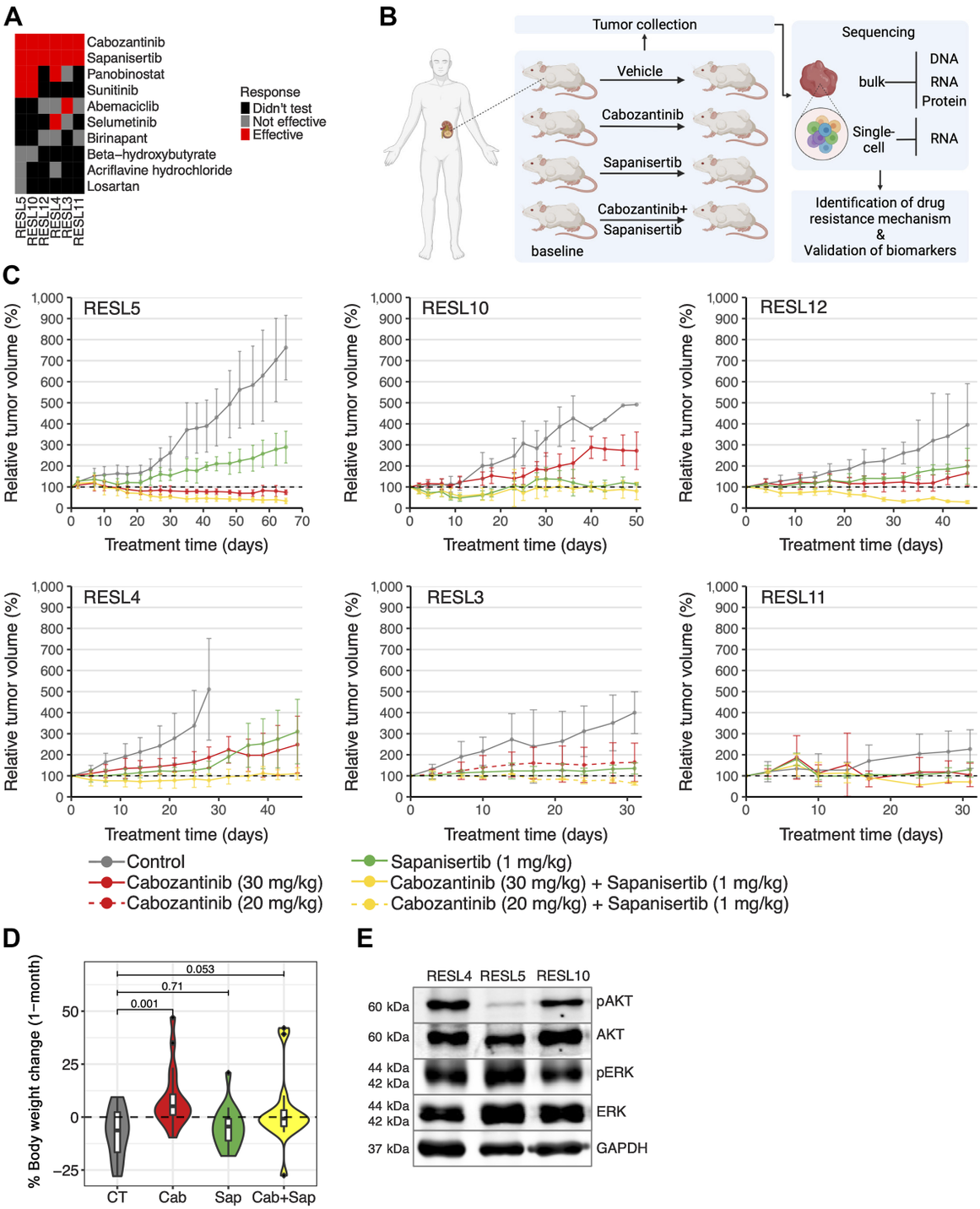

Figure 1.

Study design and PDX relative tumor volume curves. **A,** Heat map summary of the treatment response for the single drug tests across six PDX lines. **B,** Schematic illustration of the study design. **C,** Line plots depicting the relative tumor volumes of mice treated with vehicle, cabozantinib, sapanisertib, and the combination (cabozantinib plus sapanisertib) in 6 PDX lines. Relative tumor volume is calculated by normalizing the tumor volume to its initial value at day 0 (expressed as 100%). Each treatment regimen included a specific number of mice: RESL5 and RESL4 models had four mice per regimen, and RESL3 and RESL12 models had three mice per regimen. In the case of RESL10, the control group comprised five mice, while the other groups had four mice each. RESL11 consisted of four mice in the control group and three mice in each of the other groups. **D,** Bodyweight changes (compared to day 0) for the six PDX lines (mice) treated with vehicle (CT; $n = 17$), cabozantinib (Cab; $n = 19$), sapanisertib (Sap; $n = 17$), and the combination (Cab+Sap; $n = 17$). *P* values were derived from the Wilcoxon test. **E,** Western blot analysis of pAKT (Ser473), total AKT, pERK1/2 (Thr202/Tyr204), total ERK1/2, and total GAPDH using untreated PDX tumor samples of RESL4, RESL5, and RESL10.

Cryopulverization and DNA/RNA extraction

Cryopulverization was performed using Covaris CP02 CryoPrep Pulverizer and RNA extraction was performed as described by Zhou and colleagues (30). Genomic DNA was extracted with the QIAamp DNA Mini Kit (Qiagen, 51304). Total RNA was run on TapeStation (Agilent Technologies) and samples with RNA integrity number equivalent (RINe) greater than 7 were subjected to RNA sequencing.

Whole-exome sequencing

As previously described by Zhou and colleagues (30), genomic DNA (100–250 ng) was initially fragmented into 250-bp inserts using a Covaris LE220 instrument. Subsequently, automated dual-indexed libraries were generated using the KAPA Hyper Library Prep Kit (Roche) on the SciClone NGS platform (Perkin Elmer). Prior to hybrid capture, up to ten libraries were pooled in equimolar amounts by mass to create a 5-μg library pool. This library pool was then subjected to hybridization using the xGen Exome Research Panel v1.0 reagent (Integrated DNA Technologies). Hybridization was carried out for 16–18 hours at 65°C, followed by a stringent wash to remove nonspecifically bound library fragments. Enriched library fragments were subsequently eluted from the capture reagent. The enriched libraries were amplified with the KAPA HiFi master mix (Roche). To quantify the concentration of each captured library pool accurately, qPCR was performed using the KAPA Library Quantification Kit (Roche). This step ensured the generation of cluster counts suitable for the Illumina NovaSeq-6000 instrument. Finally, 2× 150 paired-end reads were sequenced to target 12 Gb of sequence data, achieving approximately 100X coverage per library.

RNA sequencing

As previously described by Zhou and colleagues (30), library preparation commenced with 0.1–0.5 μg of total RNA. Ribosomal RNA was specifically blocked utilizing FastSelect reagents from Qiagen during complementary DNA (cDNA) synthesis. The RNA underwent fragmentation within reverse transcriptase buffer with FastSelect reagent, following this thermal cycling profile: 94°C for 5 minutes, 75°C for 2 minutes, 70°C for 2 minutes, 65°C for 2 minutes, 60°C for 2 minutes, 55°C for 2 minutes, 37°C for 5 minutes, and 25°C for 5 minutes. Subsequently, mRNA was reverse transcribed into cDNA using the SuperScript III RT enzyme from Life Technologies, following the manufacturer's instructions, along with random hexamers. A second-strand reaction was then executed to produce double-stranded cDNA (ds-cDNA). The cDNA molecules were blunt-ended and had an A base added to their 3′ ends. Following this, Illumina sequencing adapters were ligated to both ends of the cDNA fragments. These ligated fragments underwent 15 cycles of amplification using primers that incorporated unique dual index tags. Finally, the prepared fragments were sequenced on an Illumina NovaSeq-6000 platform, producing paired-end reads extending 150 bases each.

Immunofluorescence staining of formalin-fixed paraffin-embedded slides

Formalin-fixed paraffin-embedded (FFPE) slides were dewaxed and rehydrated. Antigen retrieval was performed in a pH 9 Tris EDTA buffer (Genemed, 10–0046) at 80–90°C for 22 minutes. After two 9-minute incubations in 100 mmol/L glycine, two 2-minute incubations in PBST were performed. Sections were blocked for 1 hour in 10% normal donkey serum with 1% BSA/PBS. Next, primary antibodies (CA9, NB100–417, 1:800; Ki67, 14–5698–82, 1:100; CD31, AF3628, 1:100), diluted in the blocking buffer, were applied to the sections and incubated at 4°C overnight. The next day, the slides were washed twice for 5 minutes in 1× PBST and incubated with secondary antibodies at room temperature for 1 hour. Following two PBST washes, sections were stained with Hoechst (1:2,000) for 8 minutes, washed in PBS twice for 3 minutes, mounted in an aqueous mounting medium, covered with a coverslip, sealed with nail polish, and either imaged immediately or stored at 4°C for later use.

Immunoblotting

Flash-frozen tissues were washed with 1× PBS, submerged in RIPA buffer [#9806, Cell Signaling Technology (CST)] supplemented with protease (#05892791001) and phosphatase (#04906837001) inhibitor cocktail from Roche, lysed, and centrifuged at 13,300 rpm for 15 minutes. Equal amounts of proteins were loaded and separated on polyacrylamide gels, transferred onto the polyvinylidene difluoride membrane (Immobilon-FL #IPFL00010 Millipore), and blocked using an Odyssey blocking buffer. Primary antibodies used are from CST: p-MET rabbit mAb (Tyr1234/1235) #3077S 1:1,000; total MET mouse mAb #3148S 1:1,000; p-AKT rabbit mAb (Ser473) #4060S 1:1,000; total AKT rabbit #9272S 1:1,000; p-Erk1/2 rabbit mAb (Thr202/Tyr 204) #4370S 1:1,000; total Erk1/2 rabbit #9102S 1:1,000; GAPDH rabbit mAb #5174S 1:2,000) were incubated overnight at 4°C and next day were incubated with LI-COR IR 680 #926–68072 (donkey anti-mouse) and IR800 #926–32213 (donkey anti-rabbit) antibodies at 1:10,000. Imaging was done using the Bio-Rad Chemidoc MP Imaging System.

Raw reads filtering and mouse reads filtering

As previously described by Sun and colleagues (31), The initial processing of whole-exome sequencing (WES) and RNA-sequencing (RNA-seq) data involved adapter trimming and the removal of poor-quality reads using Trim Galore (v0.5.0; www.bioinformatics.babraham.ac.uk/projects/trim_galore). For PDX model sequence data, the filtering of mouse-derived reads in both WES and RNA-seq data was performed using Disambiguate (v1.0; ref. 32) with reference genomes for both mouse (GRCm38, GENCODE vM19) and human (GRCh38, GENCODE v29). Subsequently, the resulting WES reads were deduplicated and converted to BAM format utilizing Samtools (v1.5), Picard (v2.20.1), and BWA-MEM (v0.7.17). These processed reads were prepared for downstream analyses.

Somatic mutation calling

As previously described by Sun and colleagues (31), somatic mutations were identified using the SomaticWrapper pipeline (v1.5, source: github.com/ding-lab/somaticwrapper), which integrates four somatic variant calling tools: Strelka (v2.9.2; ref. 33), Mutect (v1.1.7; ref. 34), VarScan (v2.3.8; ref. 35), and Pindel (v0.2.5; ref. 36). Candidate somatic mutations underwent quality filtering using bam-readcount (source: github.com/genome/bam-readcount) with parameters –q 10 –b 20. High-confidence mutation calls were derived by retaining mutations supported by a minimum of 2 callers and meeting the following criteria: at least 14 total reads in the tumor and at least 8 in the normal. In addition, mutations observed in fewer than 4 reads and those with variant allele fractions (VAF) below 0.05 in tumor or above 0.01 in normal were excluded from the analysis.

Additional filtering in somatic mutations

As previously described by Sun and colleagues (31), to enhance the reliability of human somatic variant calls, particularly in PDX samples, which tend to have a higher incidence of false-positive

mutation sites due to mouse homologous reads, we implemented the following steps:

(i) Somatic mutations in PDX samples were retained if they were also reported in COSMIC (v90, source: https://cancer.sanger.ac.uk/cosmic) or the TCGA Cohort (source: https://gdc.cancer.gov/about-data/publications/mc3-2017).
(ii) Calls in PDXs that had corresponding human tumors were kept if the variant was found in both the PDX sample and the human tumor, regardless of its presence in the COSMIC database.
(iii) Point mutations located in the vicinity of indel regions (window size: 20 bp) were excluded from the analysis to reduce potential false positives arising from sequencing or alignment errors in low mappability regions

Gene expression quantification

As previously described by Sun and colleagues (31), we used Kallisto (v0.44.0; ref. 37) with default parameters for the estimation of transcript abundance. This was accomplished using the GENCODE transcript reference (release 29, GRCh38). Subsequently, gene expression at the transcript level was quantified using the R package "tximport" (v1.12.0; ref. 38).

Proteomics sample processing and data analysis

All samples for the proteomics study were prospectively collected as described above and processed for mass spectrometric (MS) analysis at Johns Hopkins University (Baltimore, MD). The protein extraction and tryptic digestion and electrospray ionization-liquid chromatograph (ESI-LC)/MS-MS for global proteome analysis were performed as described in Li and colleagues (39). All Data-independent acquisition (DIA) files of the global proteome were analyzed via a library-free directDIA approach embedded in Spectronaut (version 14.10, Biognosys) with precursor and protein q value cutoff set at 1%. Forty raw files acquired from 1 μg injections were analyzed together in one directDIA search. The phospho analyses were conducted by searching global DIA data with phospho modification via the directDIA approach. We applied the software function "Cross Run Normalization" normalized by the median at the peptide level, as described by Callister and colleagues (40). The resulting quantified protein and phosphorylation spectral intensity values were $\log_2$ transformed. The protein abundance level was further quantile normalized using the preprocessCore R package (41). Global proteomics data for the independent ccRCC samples were downloaded from the Clark and colleagues ccRCC study (42). The comparison of the protein abundance level between different treatment groups was performed using paired Student t test (paired by model). The FDRs were calculated using Benjamini–Hochberg FDR correction. For over-representation tests, we used the hallmark gene set and the canonical gene set from MSigDB (43), and the enricher function from the clusterProfiler R package (44).

snRNA-seq data quantification and analysis

The single-nucleus isolation and 10X library preparation and sequencing are performed as described in Wu and colleagues (45). First, a combined human (GRCh38) and mouse genome (mm10) reference was made using Cell Ranger (v5.0.1) mkref functionality. The raw snRNA-seq FASTA files were first aligned to the human-mouse reference using the Cell Ranger count function (specifying –include-introns) to generate the barcode classification (from gem_classification.csv), which classifies each barcode as either mouse cell, human cell, or multiplet. Then the FASTA files were aligned to the human-only reference using Cell Ranger. The resulting gene-by-cell UMI count matrix was used to construct a Seurat object for each sample (Seurat v.3.1.0; ref. 46). Mouse cells and multiplets were filtered out based on the gem_classification.csv. Similarly, for the mouse-only Seurat object, the FASTA files were aligned to the mouse-only reference, and the resulting count matrix was used to construct the Seurat objects. Doublets were filtered using Scrublet (https://github.com/AllonKleinLab/scrublet), which was run on each sample specifying: expected_doublet_rate = 0.06, min_counts = 2, min_cells = 3, min_gene_variability_pctl = 85, n_prin_comps = 30. The doublet score threshold was adjusted manually, which can separate the two peaks of a bimodal simulated doublet score histogram. We applied quality filters to exclude barcodes falling into specific categories: those potentially representing debris, characterized by either too few expressed genes (<200) or insufficient UMIs (<1,000); those that might correspond to more than one cell, displaying excessive gene expression levels (>10,000) or a high number of associated UMIs (>80,000); and those indicative of possible dead cells, where mitochondrial gene expression relative to total transcript counts exceeded 10%. Each cell was scored on the basis of the cell-cycle S-phase and G_2–M phase gene markers from https://raw.githubusercontent.com/hbc/tinyatlas/master/cell_cycle/Homo_sapiens.csv using the CellCycleScoring function from the Seurat package. To create a Seurat object for each sample, we applied the "SCTransform" function for scaling and normalization, which served to mitigate batch effects. Specifically, we included the following parameters: "vars.to.regress = c("mitoRatio", "nFeature_RNA", "nCount_RNA", "S.Score", "G2M.Score")" and "variable.features n = 2,000". This same scaling and normalization procedure was consistently applied during any merged analysis or subsequent cell/sample subsetting. For cell clustering, the original Louvain algorithm (47) was used, utilizing the top 30 principal component analysis (PCA) dimensions. This clustering process involved the "FindNeighbors" and "FindClusters" functions with a resolution parameter set to 0.5. Any integrated analysis underwent the same scaling and normalization. The resulting objects were then merged and integrated using SelectIntegrationFeatures, PrepSCTIntegration, FindIntegrationAnchors, and IntegrateData for subsequent analysis.

Pathway gene signatures were curated from the "hallmark" and "canonical" pathways from the C2 collection, and GO Biological Process subset of the C5 collection within MSigDB. Single-cell signature scores were calculated using Vision package v3.0.0 using the human-cell Seurat object. Signatures that were highly autocorrelated within the clusters were evaluated by Geary C, using 1− Geary C for autocorrelation effect size and computation of an empirical P value with FDR correction within Vision for significance.

Data availability

The data generated in this study are available in the Cancer Data Service (CDS; https://dataservice.datacommons.cancer.gov/#/data) under the Washington University PDX Development and Trial Center (dbGaP study accession phs002305). All other raw data generated in this study are available upon request from the corresponding author. The CPTAC proteomics data analyzed in this study were obtained from Proteomic Data Commons at https://pdc.cancer.gov/pdc/study/PDC000127. Code and associated data were deposited in Code Ocean and is available at https://codeocean.com/capsule/1970750/tree/v1.

Results

Study overview

We applied ten drugs to a set of six RCC PDX models based on an analysis of gene expression differences in ccRCC (Supplementary

Fig. S1) and previous studies (clinical and genetic features of models and corresponding patient treatments are in Supplementary Tables S1–S3; refs. 48, 49). We tested RTK inhibitors cabozantinib (targets VEGFRs, c-MET, RET, KIT, and AXL) and sunitinib (targets VEGFRs and PDGFRβ), mTOR inhibitor sapanisertib (targets mTORC1 and mTORC2), HDAC inhibitors panobinostat (targets a broad spectrum of HDACs) and beta-hydroxybutyrate (BHB; expected to have HDAC inhibitor and other effects), HIF inhibitor acriflavine hydrochloride (ACF; targets HIF1α and HIF2α), CDK inhibitor abemaciclib, MEK inhibitor selumetinib (AZD6244, ARRY-142886), IAP inhibitor birinapant, and angiotensin receptor blocker losartan potassium (**Fig. 1A**). The targeted proteins and phosphoproteins of these drugs all showed some level of upregulation in the CPTAC ccRCC cohort (Supplementary Fig. S1A), except for losartan potassium. We selected cabozantinib and sunitinib, both FDA-approved for RCC, with a view to combination testing. We chose the rest of the ten drugs as they either did not show strong activity by themselves in RCC clinical trials (panobinostat and sapanisertib), are still being investigated in RCC (abemaciclib, BHB, selumetinib, losartan), or have not been tested in RCC (ACF, birinapant), but show potential for enhanced efficacy when combined with another targeted agent.

Of all ten drugs applied singly, only cabozantinib and sapanisertib inhibited tumor growth (compared with the control) in all six PDX models (**Fig. 1A**) and, in some cases, caused tumor volume to decrease. This promising result prompted us to test the combined effects of these two drugs compared with the single treatments, as well as various combinations of cabozantinib with other drugs (Supplementary Fig. S2). However, none of the alternative combinations exhibited a comparable tumor-inhibiting effect to that observed with cabozantinib plus sapanisertib. We subsequently focused on the cabozantinib plus sapanisertib combination, performing multi-omics analyses to explore further the mechanisms underlying tumor response (**Fig. 1B**).

PDX treatment responses to cabozantinib and sapanisertib

Cabozantinib treatment resulted in a response in all six models compared with the control group (**Fig. 1C**). Tumor volumes in the cabozantinib-treated group were lower than those in the control group after 1 month of treatment, with significant differences in four models: RESL4, RESL5, RESL10, and RESL12 (Supplementary Table S4; FDR < 0.1). While cabozantinib caused significant tumor regression in RESL5, it only slowed the tumor growth rate in RESL10. Upon closer examination at days 47/48, cabozantinib resulted in tumor regression in RESL5 with a relative tumor volume (RTV; normalized the tumor volume to its initial value at day 0) of 75.8% ($P < 0.05$), but allowed tumor growth in RESL10 with an RTV of 274.2% ($P > 0.05$; Supplementary Tables S4 and S5), resulting in a tumor growth inhibition (TGI; see Materials and Methods for calculation) of 84.6% and 43.8% in RESL5 and RESL10, respectively, relative to the control (Materials and Methods). On the other hand, sapanisertib showed a reverse relative treatment efficacy in RESL5 and RESL10 compared with cabozantinib. Specifically, RESL10 showed tumor growth arrest to sapanisertib with an RTV of 121.2% ($P > 0.05$; TGI = 75.1%), while RESL5 showed sustained tumor growth with an RTV almost twice larger than that of RESL10 (RTV = 212.0%, $P < 0.05$; TGI = 57.1%) on days 47/48. This distinct drug response difference pointed to RESL5 and RESL10 as suitable for further studying the molecular mechanisms underlying differential responses to these drugs, especially cabozantinib resistance and sapanisertib resistance.

When we combined cabozantinib and sapanisertib, all six models showed lower average RTV after the combinational therapy compared with the controls after 1 month of treatment (**Fig. 1C**; Supplementary Tables S4 and S5). Specifically, five of six models (RESL3/4/5/10/12) showed significantly lower RTVs compared with controls on days 27–31 (FDR < 0.1). Moreover, all six models also showed lower average RTV after combinational therapy compared with either cabozantinib or sapanisertib alone (**Fig. 1C**). The combination therapy was significantly more effective than cabozantinib alone (FDR < 0.1) for four of the five models (with data points ≥ 2; RESL4/5/10/12) on days 27–31. Similarly, the combination therapy was significantly more effective than sapanisertib alone (FDR < 0.1) for four of the five models (with data points ≥ 2; RESL3/4/5/12) on days 27–31. Furthermore, the combination of cabozantinib and sapanisertib appears to be well-tolerated and did not induce significant weight loss compared with the control (**Fig. 1D**), an important finding considering toxicity is usually a significant concern for combinational therapy. After 1.5 months of treatment (days 47–49), RESL12 and RESL5 treated with the combination showed tumor regression, whose RTVs were 27.8% and 42.7%, respectively, while RESL10 and RESL4 only showed tumor stabilization (RTV = 88.9% and 110.0% respectively). RESL5 and RESL12 had significantly lower RTVs compared with cabozantinib alone and sapanisertib alone (FDR < 0.1). It should be noted that the number of data points decreased during the treatment period due to mouse death or euthanasia, as per the protocol.

We also identified potential connections between treatment responses and clinical and genetic features of the PDX models. RESL10 was derived from a patient who relapsed after a 10-month combined treatment of axitinib (targets VEGFRs) plus avelumab (targets PD-L1), followed by a 2.5-month cabozantinib treatment and a second relapse before tumor collection (Supplementary Table S3). RESL4 was derived from a patient receiving lenvatinib (targets VEGFRs) and everolimus (targets mTORC1) concurrent with the tumor collection (Supplementary Table S3). The other four patients had no recorded targeted or immunotherapy before tumor collection. It seems possible that prior VEGFR-targeted therapy induced the acquired resistance to cabozantinib in RESL10 and RESL4 (**Fig. 1C**). In addition, the patient whose tumor was used to derive RESL4 had been taken off lenvatinib plus everolimus treatment due to adverse events/side effects (Supplementary Table S3). As cabozantinib plus sapanisertib was effective for RESL4 (**Fig. 1C**), this combination could be a good alternative (or second line) to lenvatinib plus everolimus for a different side-effect profile and/or efficacy. We also observed that RESL10 carries a "hotspot" *PIK3CA* mutation (H1047R) and RESL4 carries a *PIK3CA* D350G mutation (Supplementary Table S2). RESL10 and RESL4 both displayed an increased abundance of phosphorylated AKT (Ser 473), which indicates the increased activation of the PI3K signaling pathway compared with RESL5 (**Fig. 1E**). This observation aligns with the fact that PI3K can activate mTORC2 and indirectly target AKT-S473 (50). This is interesting because the *PIK3CA* H1047R mutation is associated with cabozantinib resistance in NIH3T3 fibroblast cells and head and neck cancer cells (51), which is consistent with observations in our RCC PDX model RESL10. On the other hand, RESL10 showed the lowest RTV to sapanisertib, which is consistent with the PIK3CA H1047R mutation being sensitive to sapanisertib (52). For RESL4, although it also carries a PIK3CA-activating mutation, its response to sapanisertib alone is relatively less drastic, potentially due to the partial resistance developed from its previous everolimus (mTORC1 inhibitor) treatment (Supplementary Table S3). It is still unclear how such partial resistance might have developed. Nevertheless, the addition of cabozantinib, either directly through cancer cell–autonomous effects from the inhibition of RTKs it targets, or indirectly through its suppressive effects on angiogenesis, significantly enhanced the efficacy of sapanisertib in this PDX line (**Fig. 1C**).

Cabozantinib and sapanisertib combination reduces the vascular density

To further understand the histopathological features of the six PDX lines, we performed hematoxylin and eosin (H&E) staining on collected tumor samples (**Fig. 2A**). As shown in Supplementary Table S1, RESL3, RESL4, RESL5, and RESL12 are T2–T3 ccRCCs, RESL10 is a ccRCC line with sarcomatoid and rhabdoid features, and RESL11 is papillary renal cell carcinoma. When comparing the morphology among these models, we found that RESL3 and RESL5 exhibited typical clear cell characteristics, while RESL10 and RESL11 showed representative sarcomatoid and papillary structures, respectively. In concordance with the distinct drug responses we identified between RESL5 and RESL10, these two lines also showed the most differential architectural patterns in histology. RESL5 exhibited a low-grade, classical nested clear cell pattern, with the optically transparent cytoplasm and a rich capillary vascular network enclosing the cells (**Fig. 2B**). For RESL10, spindle-shaped nuclei underscored classical sarcomatoid features, as indicated by the triangles in **Fig. 2B**. Furthermore, by applying immunofluorescence staining, the positivity for Ki67 highlighted the proliferating spindle-shaped nuclei, which were costained with anti-carbonic anhydrase (CA9) within the same cells (**Fig. 3A**). In comparison to RESL10, the majority of the nuclei in RESL5 were round-shaped, and there was significantly higher expression of CA9 on the cell membrane.

To investigate the impact of cabozantinib and sapanisertib on vascular density, we examined RESL5 and RESL10 models more closely, as cabozantinib has previously demonstrated antiangiogenic effects (53). Immunofluorescence staining with CD31 was performed on control and treated RESL5/10 samples (at one month; one sample each) to assess vascular changes. RESL10 revealed the presence of a well-developed vascular network (**Fig. 3B**; Supplementary Fig. S3A and S3B), which was somewhat difficult to discern in H&E staining. Subsequently, we compared CD31 expression densities between the control and treated groups. Cabozantinib treatment significantly reduced vascular density in both RESL5 and RESL10 (**Fig. 3B** and **C**; Supplementary Fig. S3A–S3B), whereas sapanisertib treatment

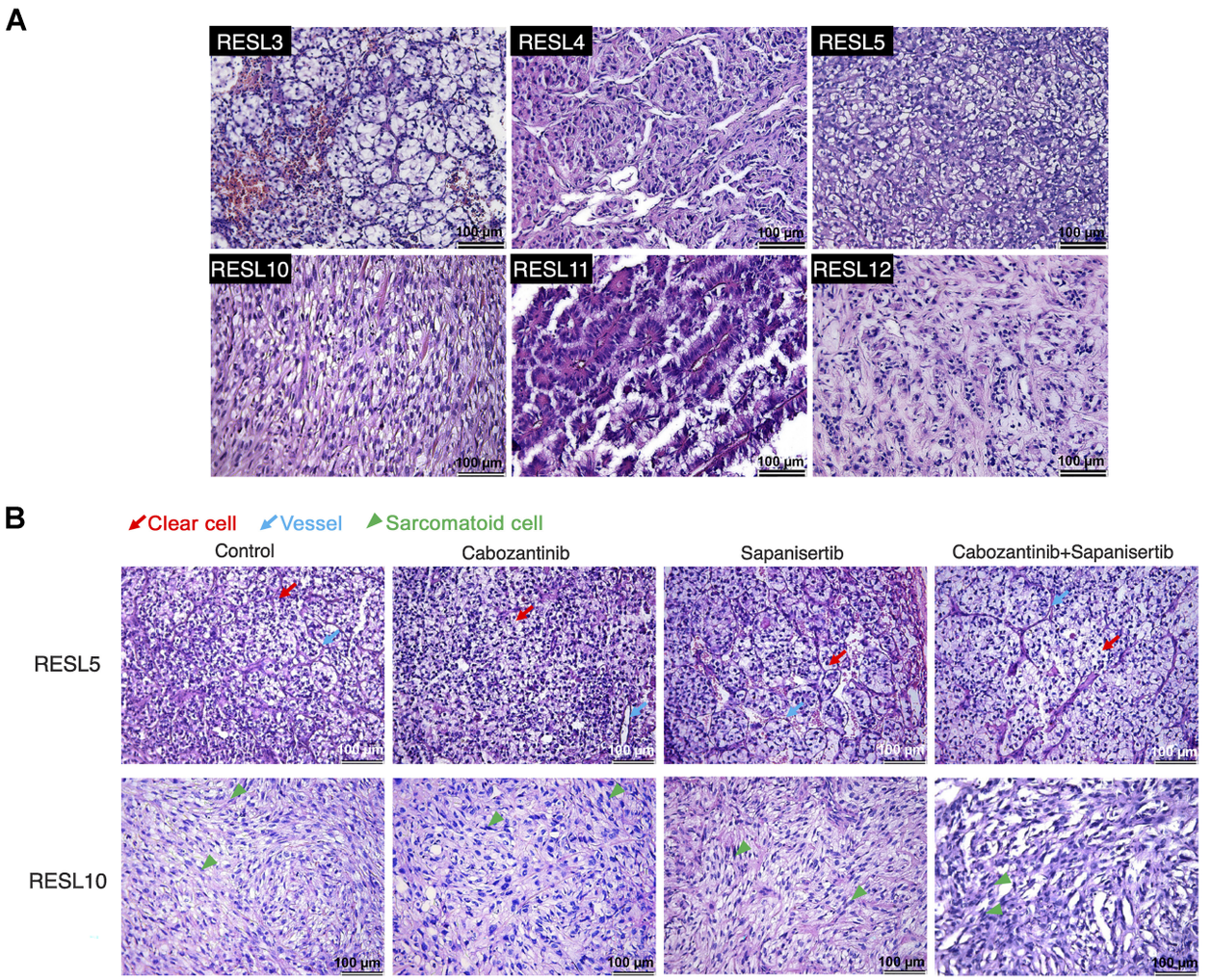

Figure 2.

H&E images for the PDX models. **A,** Representative H&E images for the six PDX models. **B,** Representative H&E images for tumors in mice treated with vehicle, cabozantinib, sapanisertib, and the combination (cabozantinib plus sapanisertib) in PDX lines RESL5 and RESL10. Red arrows, clear cells; green arrows, sarcomatoid cells; blue arrows, vessels.

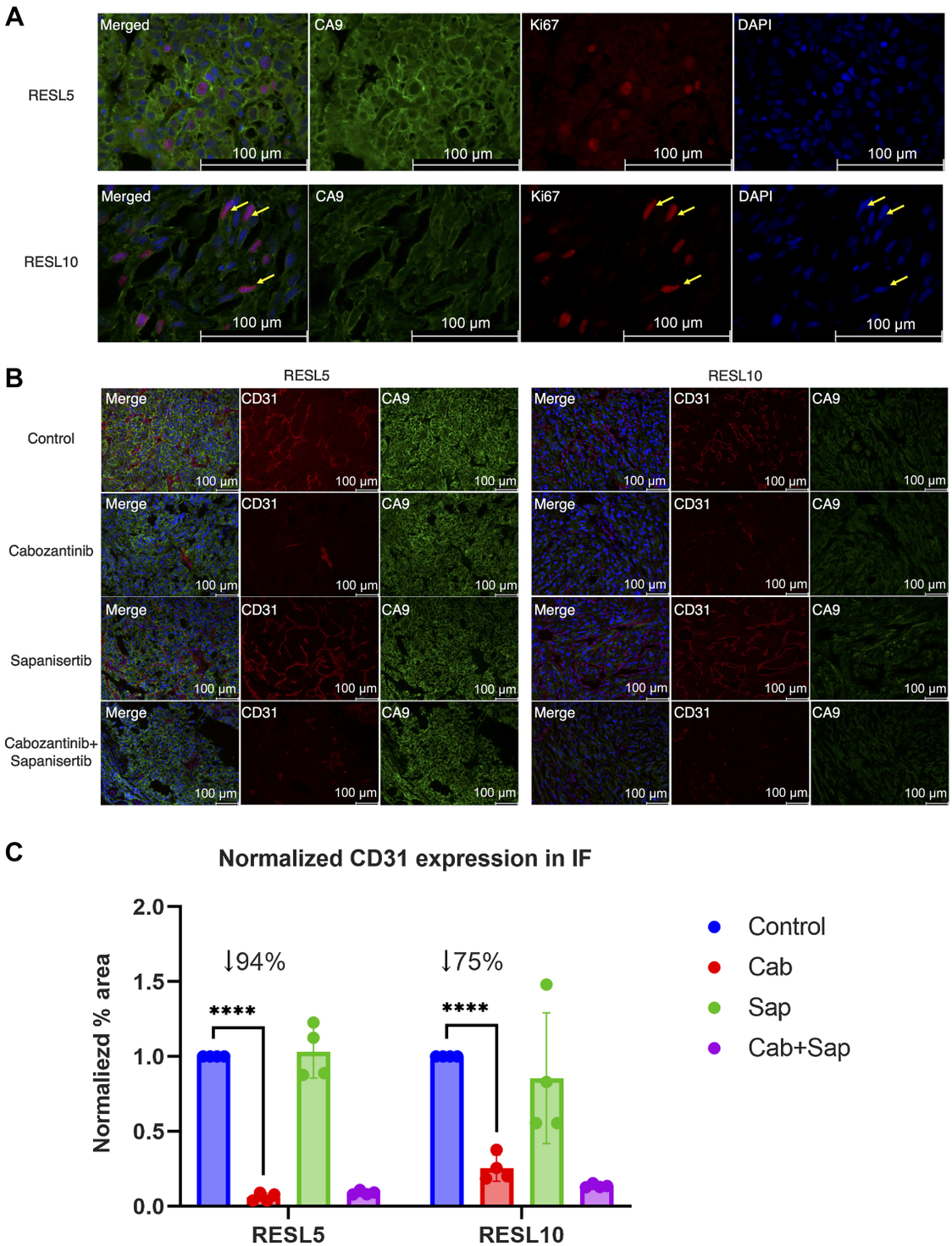

Figure 3.

Immunofluorescence staining for tumor cells and vasculature in PDX lines RESL5 and RESL10. **A,** Representative IF images of untreated tumor samples stained with anti-CA9 antibody (green), anti-Ki67 antibody (red), and DAPI (blue) for PDX lines RESL5 and RESL10. Scale bars, 100 μm. **B,** Representative immunofluorescent images of tumor samples stained with anti-CD31 antibody (red) and anti-CA9 antibody (green) in mice treated with vehicle, cabozantinib, sapanisertib, and the combination (cabozantinib plus sapanisertib) in PDX lines RESL5 and RESL10. Three independent experiments were performed with similar results. Scale bars, 100 μm. **C,** Bar plot showing the normalized CD31 expression from immunofluorescent images for mice treated with vehicle, cabozantinib, sapanisertib, and the combination in PDX lines RESL5 and RESL10. ****, $P < 0.0001$ using Student t test.

did not result in apparent changes in vessel densities. This aligns with cabozantinib's ability to inhibit the tyrosine kinase activity of MET, VEGFRs, and other receptors that play crucial roles in tumor angiogenesis. Sapanisertib, as an mTOR inhibitor, exerts a comparatively lesser effect on angiogenesis than cabozantinib. Furthermore, when cabozantinib and sapanisertib were administered in combination, the reduction in vessel density remained evident, suggesting that sapanisertib does not interfere with the antiangiogenic effects of cabozantinib. Finally, quantifying CD31 expression density revealed that RESL5 exhibited a higher responsiveness to cabozantinib than RESL10 (**Fig. 3C**; $P < 0.0001$). Following cabozantinib treatment, the expression density of CD31 decreased by 94% in RESL5 compared with the control, while RESL10 showed a 75% reduction. These results align with the observation that RESL5 exhibited better tumor inhibition in response to cabozantinib compared with RESL10 (**Fig. 1C**).

Cabozantinib plus sapanisertib treatment inhibits cell cycle–related proteins while inducing proteins related to epithelial–mesenchymal transition

To obtain a mechanistic understanding of the observed tumor regressions after cabozantinib–sapanisertib cotreatment, we collected tumors under four treatment regimens conducted for identical durations, namely vehicle control, cabozantinib, sapanisertib, and the combination therapy. We subsequently conducted bulk WES, bulk RNA-seq, global proteomics, and phosphoproteomics data searching from global data, and single-nucleus RNA-seq (snRNA-seq) on 8 samples from RESL5 and RESL10 (**Fig. 1B**; Supplementary Fig. S1B).

The combination resulted in the differential expression of 310 human proteins compared to the control ($P < 0.05$, difference in $\log_2$ intensity > 0.1), including more downregulation than upregulation (97 up and 213 down; **Fig. 4A**), although statistical significance was not reached after multiple-testing correction. To identify the pathways altered by the combination treatment, we performed pathway overrepresentation tests on the differentially expressed proteins and examined the top five pathways enriched in differentially expressed proteins (**Fig. 4B**). Proteins that were downregulated were most enriched in protein translation, oxidative phosphorylation, protein localization, and E2F targets. Downregulated proteins involved in translation included many mitochondrial ribosomal proteins, such as MRPL1/3/9/11/14/16/19/41/43 and MRPS9/10/31. Many downregulated proteins were involved in oxidative phosphorylation, such as TIMM8B, GOT2, HCCS, UQCRQ, SLC25A20, NDUFB1, COX7C, TOMM22, SLC25A5, UQCRB, UQCR10, COX4I1, COX17, MRPL11, and DLD. Decreased oxidative phosphorylation indicates a reduction of ATP and cell membrane activity, which eventually lead to cell swelling and death (54). This is a potential molecular mechanism underlying the treatment effects we observed for the combination therapy. Moreover, we observed decreased protein levels of cell cycle–related targets of E2F TFs (TK1, CDK1, KPNA2, MCM2, PRDX4, PCNA, TBRG4, MCM3, RFC3, and MCM7), which may be another potential mechanistic explanation for the tumor growth arrest/regression induced by the combination treatment.

On the other hand, proteins upregulated after combination treatment were involved in the epithelial-mesenchymal transition (EMT), amino and nucleotide sugar metabolism, G_2–M checkpoint, nuclear envelope breakdown, and cellular trafficking proteins pathways (**Fig. 4B**). In particular, the combination treatment increased the protein levels of EMT pathway members TGFBI, LRP1, COL7A1, TAGLN, SCG2, THBS1, and TFPI2 compared with the control, among which LRP1 and COL7A1 also showed increased gene expression. Moreover, the combination treatment also increased the protein levels of G_2–M checkpoint proteins CDK4, TNPO2, RPS6KA5, PRMT5, and NUP98. EMT plays an important role in cancer progression, metastasis, and drug resistance (55, 56). The upregulation of EMT and G_2–M checkpoint proteins might be a survival adaptation to the blockade of RTK and mTOR signaling by the combination treatment.

Eight proteins, namely IGF2BP3, DNAJC7, PYCR1, CHMP6, MRM3, ERO1B, CLIC6, and COBLL1, showed significantly lower abundance in combination-treated tumors compared with both cabozantinib-treated and sapanisertib-treated tumors (**Fig. 4C**). Using the proteomics data from an independent ccRCC cohort (81 cases; ref. 42), we found that IGF2BP3, PYCR1, and ERO1B showed significantly higher protein levels in tumor samples than in the matching normal adjacent tissue (FDR < 1e-6, **Fig. 4D**). Moreover, Kaplan–Meier analysis showed that higher IGF2BP3 protein levels are associated with worse survival (**Fig. 4E**; $P < 0.05$). Higher baseline IGF2BP3 protein level is also associated with worse tumor growth inhibition by the combo treatment (Supplementary Fig. S4). These results suggest that IGF2BP3 might have an oncogenic role in ccRCC and that the reduced IGF2BP3 caused by combination treatment might contribute to more potent tumor inhibition than the two monotherapies.

snRNA-seq reveals treatment-associated transcriptome activities in PDX tumor cells

We performed snRNA-seq on the RESL5 and RESL10 tumors under the aforementioned four treatment regimens, as these two models showed the most contrasting treatment responses to cabozantinib and sapanisertib. After aligning the snRNA-seq data to a mouse-human combined reference and performing data processing steps, we obtained 52,845 human tumor cells and 19,117 mouse cells across eight samples (**Fig. 5A** and **B**). Mouse cells were identified as endothelial cells, fibroblasts, myofibroblasts, and macrophages based on specific cell type markers (**Fig. 5C**). RESL10 tumors exhibited a higher proportion of mouse stromal content, particularly mouse fibroblasts, compared with RESL5 (**Fig. 5D**). In line with expectations, both cabozantinib-treated tumors showed decreased percentages of mouse endothelial cells compared with the controls (**Fig. 5D**), indicating a selective targeting of endothelial cells by cabozantinib. Tumors treated with cabozantinib plus sapanisertib also displayed reduced endothelial percentages compared with the controls (<40% of the controls in both models), suggesting that the combination therapy maintained cabozantinib's effect on endothelial cells. Regarding tumor cells, cabozantinib-treated tumors had similar (RESL5) or higher (RESL10) tumor cell percentages compared with the control group (**Fig. 5D**). Conversely, sapanisertib decreased the fractions of human tumor cells in both models, indicating its primary targeting of tumor cells rather than stromal cells.

To investigate the treatment-specific effects on tumor subpopulations, we further subdivided tumor cells into 17 meta-clusters using a clustering resolution of 0.5 (**Fig. 6A**). This resolution allowed for the identification of meta-clusters with at least 50 unique markers. Analysis of the meta-clusters' expression signatures revealed 42 consistently expressed gene sets (FDR < 0.1, C > 0.1; **Fig. 6B**), primarily associated with extracellular matrix (ECM), drug metabolism, cell cycle, stress response, and translation. Some meta-clusters exhibited unique expression signatures, such as MC12, which displayed high cycling gene signatures, and MC7, which showed high stress response and translation-related signatures (**Fig. 6B**).

When examining the expression signatures of the meta-clusters within each sample, we observed that tumor cells from the same model tended to cocluster (**Fig. 6C**), indicating substantial model-specific transcriptomic differences. Within-model pairwise correlations

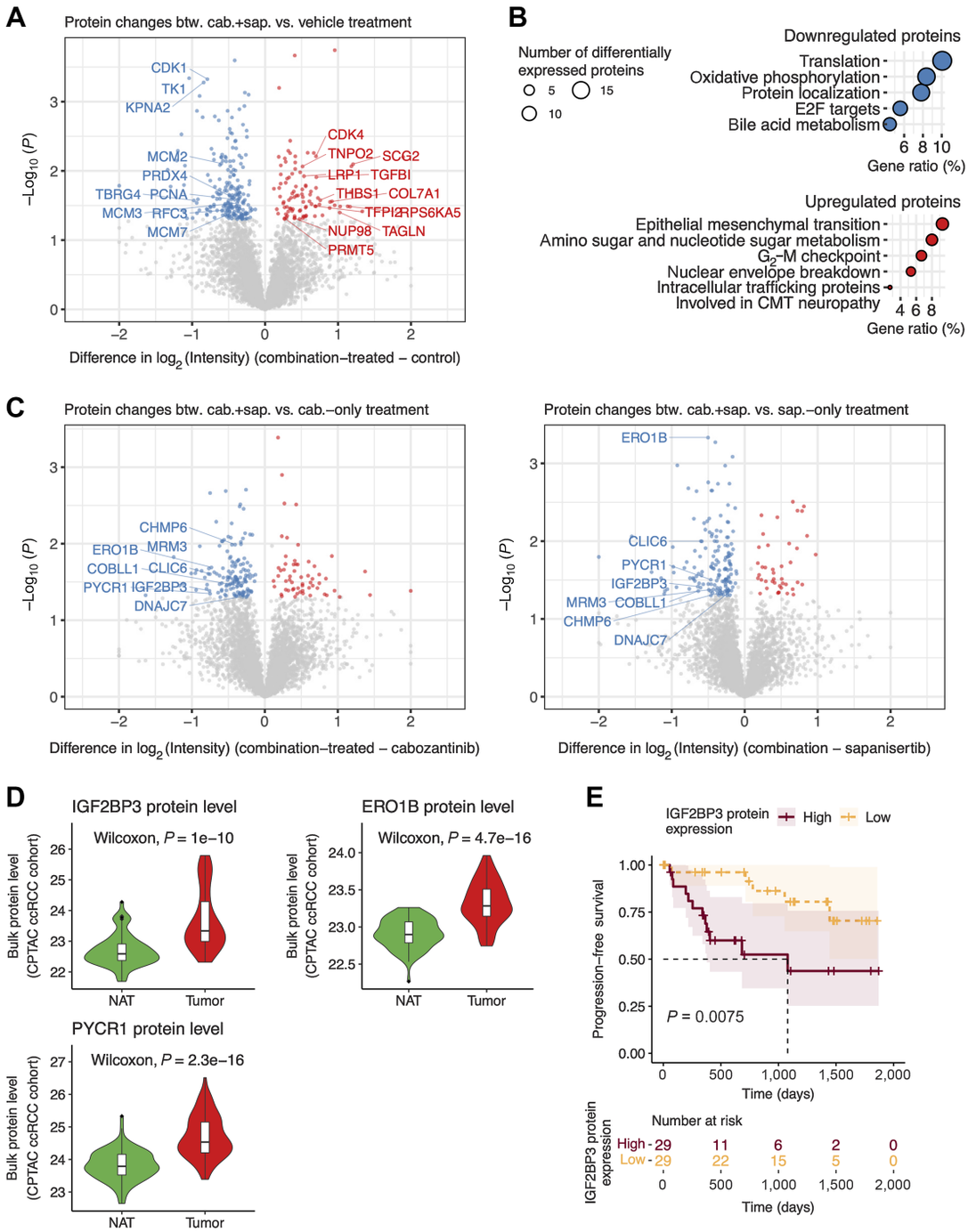

Figure 4.

Proteomic analysis of the treatment effects. **A,** Volcano plot showing differentially expressed proteins between tumors after combination treatment of cabozantinib plus sapanisertib compared with the vehicle-treated controls, mapping 97 upregulated proteins (red dots) and 213 downregulated proteins (blue dots). **B,** Dot plot showing the overrepresented gene sets in proteins downregulated (top) and upregulated (bottom) after combination treatment. **C,** Volcano plots showing differentially expressed proteins between tumors after combination treatment versus single-agent treatments. Left, combination-treated and cabozantinib-treated tumors, mapping 59 upregulated and 146 downregulated proteins. Right, the comparison between combination-treated and sapanisertib-treated tumors, mapping 42 upregulated and 154 downregulated proteins. **D,** Violin plots showing protein levels of IGF2BP3, ERO1B, and PYCR1 in the tumor and normal adjacent tissue (NAT) samples in the CPTAC ccRCC discovery cohort. **E,** Kaplan–Meier curves displaying progression-free survival probability for two groups of patients in the CPTAC ccRCC discovery cohort. The two groups of patients were selected on the basis of the IGF2BP3 protein levels in their primary tumors. High IGF2BP3 protein expression represents those with protein expression in the upper 35% quantile. Low IGF2BP3 protein expression represents those with protein expression in the bottom 35% quantile.

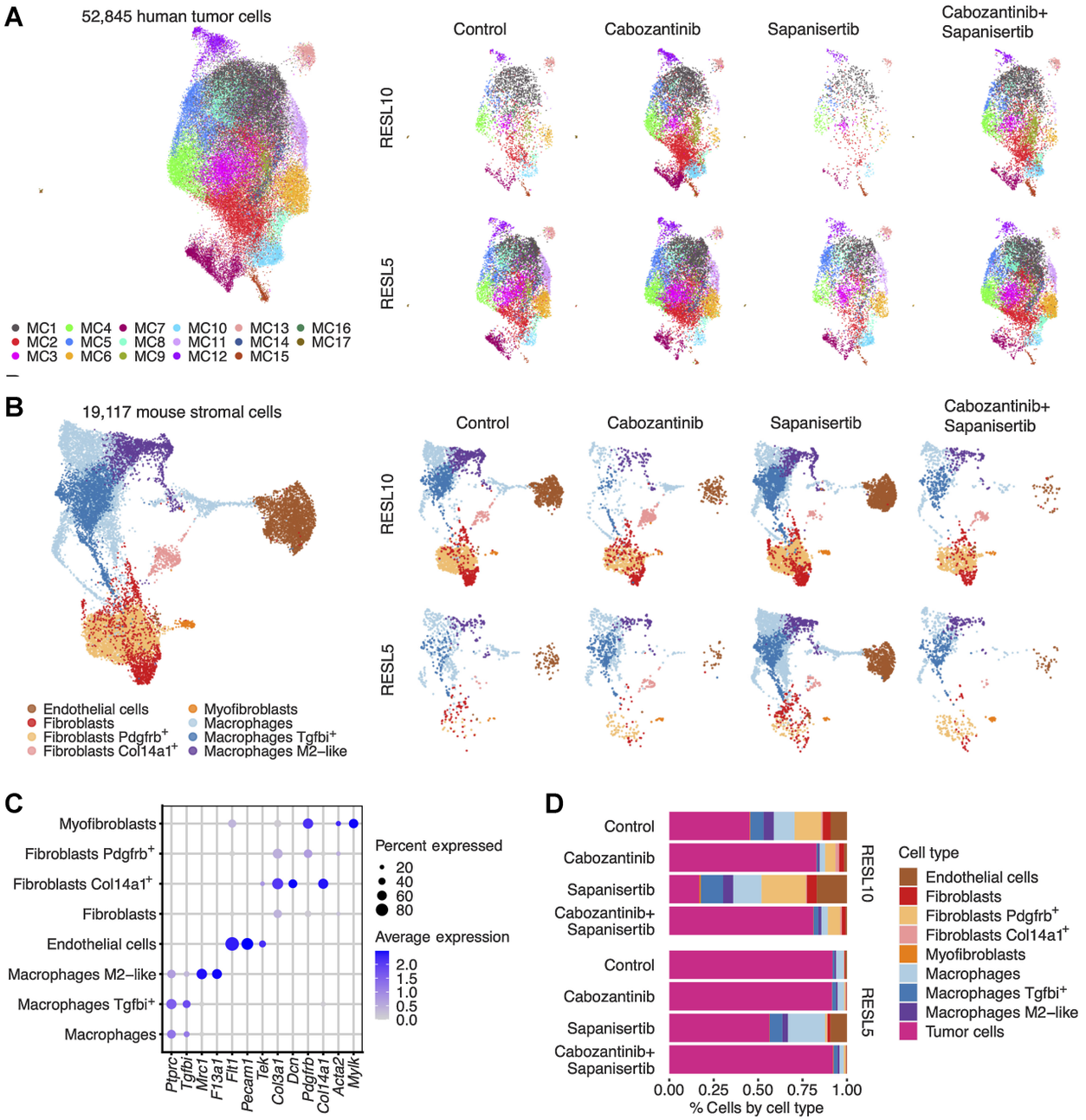

Figure 5.

Overview of snRNA-seq data. **A,** Uniform Manifold Approximation and Projection (UMAP) visualization of the human tumor cells, colored by cluster IDs. Left, all the human tumor cells from the eight samples. Right, the cells divided by sample. **B,** UMAP visualization of the mouse cells, colored by cell type. Left, all the mouse cells from the eight samples. Right, the cells divided by sample. **C,** Dot plot showing the expression of marker genes for different mouse cell types. **D,** Bar plot showing the percentage of different cell types in each of the eight samples.

among meta-clusters were generally higher than across-model correlations (**Fig. 6C**). Tumor-cell meta-clusters from RESL10 showed high signature scores for ECM-related pathways, such as the EMT pathway, while meta-clusters from RESL5 showed high signature scores for keratinization and drug metabolism by cytochrome P450 (**Fig. 6C**, right). Nonetheless, the exception is the cluster MC7, in which tumor cells from the two models showed high pairwise correlations and exhibited high signature scores for stress response (**Fig. 6C**), suggesting tumor cells with MC7-like signatures may be less unique to individual patients and could be found across different patients.

We also identified some treatment-associated changes in the tumor-cell clusters. We found that the fraction of cycling tumor cells (MC12) decreased after the combination treatment compared to control in both models, while the single-agent treatments increased the fraction

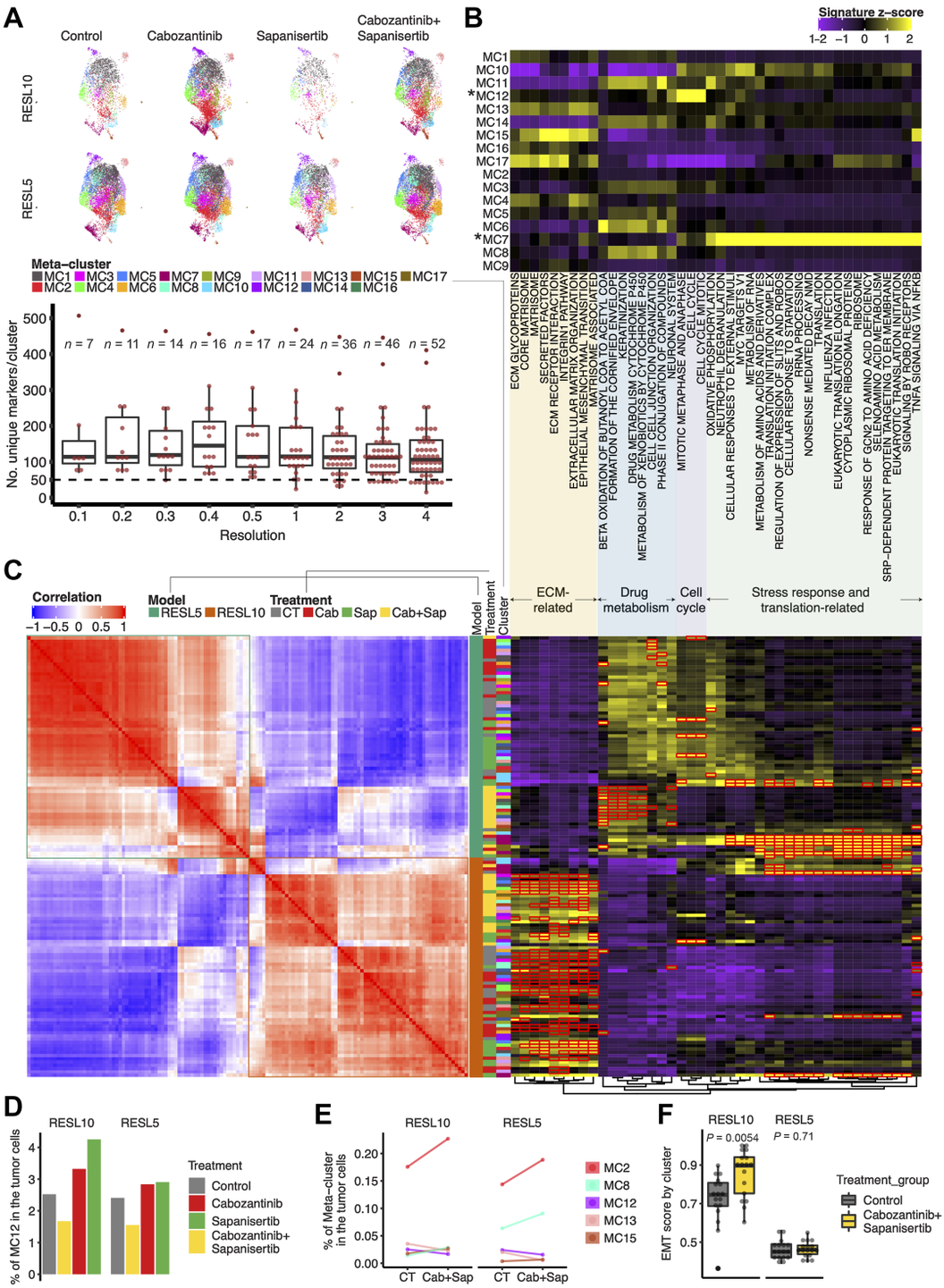

Figure 6.

Pathway activities of tumor cell clusters in treated and control tumors. **A,** Top, Uniform Manifold Approximation and Projection (UMAP) visualization of the human tumor cells, colored by meta-cluster IDs and divided by sample. Bottom, box plot showing the number of marker genes per cluster for different clustering resolutions. **B,** Heat map showing the pathway activity of each meta-cluster. **C,** Left, heat map showing the pairwise correlation coefficient of meta-cluster cells divided by different samples. Both the *x*-axis and *y*-axis represent meta-cluster cells divided by sample. Right, heat map showing the pathway activities of meta-cluster cells divided by different samples, sharing the same *y*-axis as the left and the same *x*-axis as **B**. **D,** Bar plot showing the percentage of cells in MC12 (cycling tumor cells) in each sample. **E,** Line plot showing the percentage of cells in different meta-clusters in control and combo-treated samples, colored by meta-cluster ID. **F,** Box plot showing the EMT score distribution in control and combo-treated samples.

of cycling tumor cells (**Fig. 6D**). These results suggest that these cycling tumor cells are more resistant to the single-agent treatments, and the cabozantinib plus sapanisertib combination is better at eliminating the cycling tumor cells compared with the monotherapies, as expected. Combination treatment also decreased the percentage of the tumor-cell clusters MC13, while increasing those of MC2, MC8, and MC15 (**Fig. 6E**), suggesting a treatment-specific shift in tumor subpopulations. Interestingly, we also found the EMT signature scores (median) increased across meta-clusters after the combination treatment in both models (**Fig. 6F**), especially in RESL10, consistent with what we found in proteomics data.

Baseline MET protein levels predict response to cabozantinib

To guide patient stratification and drug selection, we investigated protein and phosphorylation sites within key pathways affected by cabozantinib and sapanisertib and their association with drug responses. These proteins/pathways include RTKs and their corresponding ligands (such as MET, HGF, VEGFRs, and VEGFs), the PI3K/AKT/mTOR pathway, and the Ras/Raf/MAPK pathway (**Fig. 7A** and **B**; ref. 57). Among these, MET protein levels exhibited the highest expression in RESL10 and the lowest in RESL5. During treatment, RESL10 was the least sensitive to cabozantinib (TGI = 35.1% on day 28), whereas RESL5 was the most sensitive to cabozantinib (TGI = 65.3% on day 28). Notably, RESL10 displayed the least sensitivity to cabozantinib treatment (TGI = 35.1% on day 28), whereas RESL5 exhibited the highest sensitivity (TGI = 65.3% on day 28). We observed a negative correlation between MET protein level and cabozantinib's inhibition of tumor growth (**Fig. 7C**; $P = 0.0013$, $R = -0.97$), which was consistent with the trend observed for *MET* mRNA (**Fig. 7C**). The snRNA-seq data demonstrated higher *MET* and *HGF* levels (the ligand for MET) in RESL10 compared with RESL5 (**Fig. 7D**), and this differential expression was confirmed by Western blotting of PDX tissues (**Fig. 7E**). Collectively, these findings suggest that MET could serve as a potential biomarker for excluding cabozantinib treatment options.

Cabozantinib plus sapanisertib inhibits ERK signaling

We conducted experiments to investigate the signaling changes downstream of the targeted proteins, finding a significant reduction in pERK (T202/Y204) levels for combination treatment compared with cabozantinib treatment alone in RESL10 ($P = 0.048$), RESL5 ($P = 0.022$), and RESL12 ($P = 0.012$), with a noticeable trend

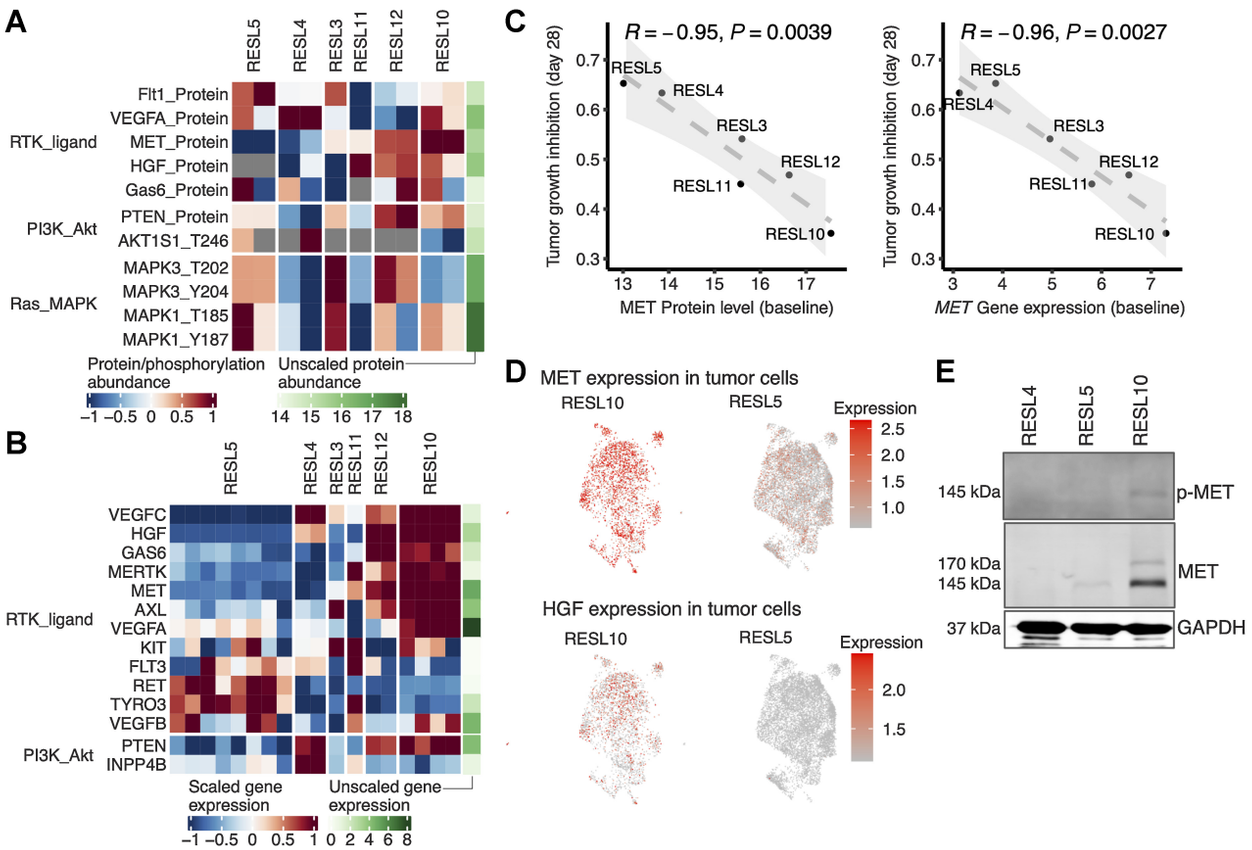

Figure 7.

Protein markers associated with treatment effect. **A,** Heat map showing the scaled protein/phosphorylation abundance of the key members in the PI3K–mTOR pathway and RTKs targeted by cabozantinib (that were detected in the proteomics and phosphoproteomics datasets) in the control tumor samples across the PDX lines. **B,** Heat map showing the scaled gene expression of the key members in the PI3K–mTOR pathway and RTKs targeted by cabozantinib in the control tumor samples across 6 PDX lines. The unscaled gene expression represents $\log_2$ (TPM+1). **C,** Scatter plot showing the association between baseline MET protein level (left) or *MET* gene expression (right) with the tumor growth inhibition at day 28. **D,** *MET* (top) and *HGF* (bottom) gene expression in the human tumor cells in the snRNA-seq data of the RESL10 and RESL5 control tumor samples. **E,** Western blot of the phospho-MET (Tyr1234/1235), total c-MET, and total GAPDH in untreated RESL4, RESL5, and RESL10 tumor samples.

observed for RESL4 (**Fig. 8A** and **B**). Similar trends were observed in the pERK to total ERK ratio. These results indicate that the addition of sapanisertib effectively restrains ERK phosphorylation when combined with cabozantinib, potentially contributing to the superior efficacy of the combination therapy compared with sapanisertib treatment alone. Furthermore, combo-treated tumors exhibited lower normalized pERK levels compared with sapanisertib-treated tumors for RESL10, RESL5, and RESL12 ($P < 0.1$), further supporting the hypothesis that suppression of ERK activation may be an important mechanism in the antitumor effects of these drugs in PDX models.

We subsequently explored the effects of combo treatment downstream of ERK signaling using bulk RNA-seq data, focusing on activities of various ERK-regulated TFs by examining the averaged expression of their known downstream targets per sample. We identified 14 TFs that exhibited lower activity scores in the combo-treated samples compared with controls ($P < 0.2$), cabozantinib-treated, and sapanisertib-treated samples, including members of the JUN (JUNB,

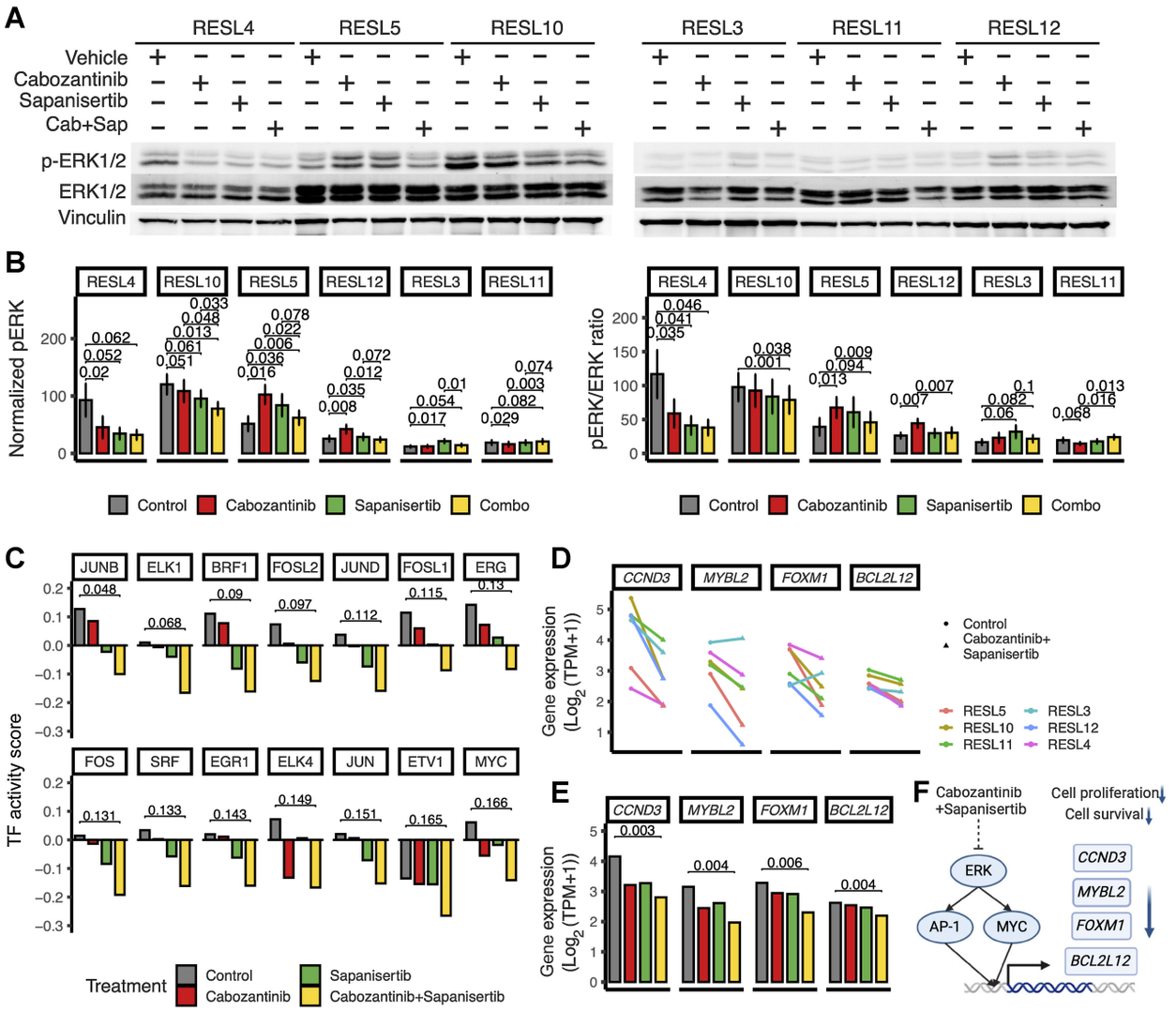

Figure 8.

Western blot analysis and mechanistic insights into pERK signaling. **A,** Representative Western blot analysis of pERK and ERK protein expression. Vinculin was used as the loading control. Ctrl, control; Cab+Sap, cabozantinib plus sapanisertib. **B,** Bar plots showing normalized densitometric analysis of pERK ($n = 4$). The phosphoprotein bands were normalized against the loading control for each lane. The ratio of phosphoprotein/total corresponding protein was calculated by dividing the density of phosphoprotein by the corresponding total protein intensity in the same experiment. Left graph, the relative expression of phosphoprotein. Right graph, the ratio of phosphoprotein/total corresponding protein. Data points represent mean ± SEM. Paired two-tailed Student *t* test. **C,** Bar plots displaying the scores of TF activities for selected TFs. Paired two-tailed Student *t* test. **D,** Line plot illustrating the normalized gene expression of selected ERK downstream genes in control and combo-treated samples. **E,** Bar plot representing the normalized gene expression of selected ERK downstream genes in control, cabozantinib-treated, sapanisertib-treated, and combo-treated samples. **F,** Illustration depicting the potential ERK signaling cascade following cabozantinib plus sapanisertib treatment. The combo treatment inhibits ERK kinase activity, resulting in decreased pERK levels. Consequently, the activities of downstream transcription factors (e.g., AP-1 and MYC) are inhibited due to the absence of phosphorylation by ERK. This leads to reduced transcription of their target genes, including those involved in cell proliferation and survival.

JUND, JUN) and FOS protein families (FOSL2, FOSL1, FOS). Notably, JUNB ($P = 0.048$) and FOSL2 ($P = 0.097$) displayed particularly reduced activity scores in the combo-treated samples (**Fig. 8C**). Although statistical significance was not reached after multiple-testing correction likely due to sample size, these findings suggest that the combo treatment impacts the activities of ERK downstream TFs.

Further examination of known target genes of ERK-regulated TFs revealed the downregulation of four genes involved in cell-cycle control and apoptosis in the combo-treated samples. Namely, *CCND3, MYBL2, FOXM1*, and *BCL2L12* exhibited lower average expression in the combo-treated samples compared to single agent-treated samples (**Fig. 8D**). The combo-treated samples also displayed lower gene expression compared with the corresponding controls (**Fig. 8E**). These findings suggest that the combo treatment affects cell proliferation and survival, at least partially, by modulating the transcriptional programs regulated by ERK signaling.

Collectively, our results provide mechanistic insights into the molecular and cellular effects of the cabozantinib plus sapanisertib combination treatment in ccRCC. The combination treatment effectively restrains ERK phosphorylation and leads to the downregulation of ERK downstream TFs and their target genes involved in cell-cycle control and apoptosis (**Fig. 8F**). These findings highlight the cabozantinib plus sapanisertib combination as a promising treatment for patients with ccRCC who are unresponsive to other treatment modalities.

Discussion

Targeted agents and ICIs have been the pillars for treating patients with RCC with inoperable or metastatic tumors, as RCCs are generally not responsive to chemotherapy or radiotherapy. Because RCCs are highly vascular, TKIs targeting VEGF signaling have been the major first-line and second-line targeted agents, but resistance eventually develops (58). Hitting multiple targets with several drugs is one method to overcome such resistance. Here we tested ten drugs and selected combinations across six RCC PDX models, finding cabozantinib and sapanisertib, as well as their combination, to be the most effective single and combinational therapies. Their combination is effective in suppressing tumors from patients who failed prior TKI and immune checkpoint inhibitors (ICI) treatments. Most importantly, the TORC1 and TORC2 double inhibitor sapanisertib is effective in countering resistance to cabozantinib.

We found various degrees of response to the drugs tested across the six lines with different mutation profiles. Interestingly, RESL10, harboring a *PIK3CA* H1047R mutation and high levels of MET, showed the least tumor inhibition by cabozantinib, despite the fact that cabozantinib targets MET in addition to VEGFR. Mutations in members of the PI3K pathway occur frequently in various human cancers, including ccRCC (59). These mutations are most commonly found in the *PIK3CA* gene, which encodes the p110α catalytic subunit of PI3K. Five percent of ccRCC tumors harbor *PIK3CA* amplifications and activating mutations (59) with hotspots at H1047 in the kinase domain and E542 and E545 in the helical domain (60, 61). Nisa and colleagues reported that PIK3CA H1047R confers resistance to MET inhibition (using tepotinib) in head and neck cancer cells and combined MET/PI3K inhibition leads to enhanced antitumor activity in these tumors compared with single-agent treatments (51). Our results are consistent with the Nisa and colleagues study, suggesting that RESL10 might be resistant to cabozantinib, partially because of its *PIK3CA* mutation–linked resistance to MET inhibition; however, when sapanisertib was added as an inhibitor of PI3K/AKT/mTOR signaling, a significant response was achieved in RESL10, demonstrating the power of rational combinational therapy in countering drug resistance in RCC treatment.

Reviewing the treatment histories of patients in our study, we identified opportunities for cabozantinib plus sapanisertib to improve patient outcomes. The RESL10 patient had received axitinib and avelumab followed by cabozantinib, but both regimens were discontinued due to disease progression. The prior TKI treatments potentially induced resistance to TKI monotherapy, which was overcome by adding sapanisertib to cabozantinib in the PDX model. Similarly, the RESL4 patient had received the FDA-approved combination lenvatinib plus everolimus, but treatment was discontinued due to adverse events. However, the RESL4 PDX model showed a positive response to cabozantinib plus sapanisertib, suggesting that this combination, with a different side-effect profile, could be an effective alternative. In addition, RESL5 and RESL3 donors discontinued target therapy or immunotherapy due to adverse events or disease progression after tumor collection, further indicating that cabozantinib plus sapanisertib could be a good alternative for patients who failed the standard of care.

In this study, we found that IGF2BP3 protein was downregulated after cabozantinib and sapanisertib combination treatment compared with single-agent therapies. IGF2BP3 is a member of the IGF2BP protein family, which is involved in RNA localization, transportation, stability, and cell metabolism, proliferation, migration, and invasion (62). IGF2BP proteins are absent in normal adult tissues, but IGF2BP3 reexpresses in various cancers, including kidney cancer (63, 64). Tissue and circulating IGF2BP3 levels predict metastasis in ccRCC (65–68), which aligns with our finding that high IGF2BP3 protein levels are associated with worse survival in the CPTAC ccRCC cohort. We found decreased IGF2BP3 proteins in RCC PDX tumors after cabozantinib plus sapanisertib treatment when compared with the single-agent–treated tumors, suggesting an explanation of the synergistic effect of cabozantinib and sapanisertib treatments. We also found a significant negative correlation between baseline IGF2BP3 protein level and tumor growth inhibition induced by the combination therapy, suggesting higher baseline IGF2BP3 protein levels exhibited a more favorable response to the combination treatment. By examining the reported IGF2BP3 targets in cancer summarized by Mancarella and colleagues (69), we found that the combination treatment decreased mRNA levels of *CCND3* compared with the control ($P < 0.05$) and cabozantinib treatment ($P < 0.05$), and trended for sapanisertib treatment ($P < 0.1$). This suggests the downregulation of IGF2BP3 and its downstream target CCND3 may be part of the mechanism by which the combo treatment achieves better outcomes.

We also found that the pyrroline-5-carboxylate reductase 1 (PYCR1) protein is downregulated after the combination treatment compared with the single-agent treatments. PYCR1 promotes EMT by inducing mitochondrial ion protease, thus activating M2 macrophage polarization and angiogenesis (70), and its upregulation is correlated with shorter overall survival (OS) in RCC (71). In ccRCC cell lines, PYCR1 is associated with resistance to multiple drugs, including TKI lapatinib (72). Cabozantinib treatment leads to an increased PYCR1 protein level compared with the control ($P < 0.05$). Interestingly, tumors treated with the combination of cabozantinib plus sapanisertib have a PYCR1 protein level similar to the control, but lower than that in either of the monotherapies. Our results indicate the cabozantinib plus sapanisertib combination limits PYCR1, thus avoiding PYCR1-mediated drug resistance. However, additional experiments are needed to validate the relevance of IGF2BP3 and PYCR1 levels in mediating the tumor inhibition effects of the cabozantinib plus sapanisertib therapy.

We found that high MET protein abundance and gene expression predict less tumor growth inhibition by cabozantinib. Cabozantinib targets many RTKs, including MET, whose elevated expression in advanced RCC has been associated with poor prognosis and prior exposure to VEGFR TKIs (10, 73). Of note, RESL10, which shows the highest MET expression, was derived from a patient who had previously received VEGFR inhibitors axitinib and cabozantinib. RESL4 was similarly derived from a patient who was undergoing VEGFR inhibitor lenvatinib plus everolimus treatment. However, its MET protein expression is lower than RESL3, RESL11, and RESL12, which had not received prior VEGFR inhibitors. In preclinical models, high MET expression is associated with resistance to VEGFR TKI treatment (74), although its level did not affect cabozantinib treatment outcomes in the phase III METEOR RCC clinical trial (11), nor in breast cancer or cholangiocarcinoma clinical trials (75, 76). However, in a more recent study of the RCC METEOR trial, decreased MET levels predicted improved progression-free survival (PFS) and OS (77). In the phase III CELESTIAL trial of cabozantinib treatment in advanced hepatocellular carcinoma, a high MET level was associated with shorter OS (78). Although our results support a prognostic value for MET levels in ccRCC treatment, additional studies are needed to confirm the relation between MET protein and cabozantinib response in RCC using larger cohorts.

Our results show that the combination of cabozantinib plus sapanisertib performs similarly to the FDA-approved lenvatinib plus everolimus combination (Supplementary Fig. S5), which is not always tolerated by patients. In fact, the patient donor for RESL4 had this combo stopped due to adverse effects. The cabozantinib and sapanisertib combination, which suppressed RESL4 tumors, has a different side-effect profile (18, 79) and could be a good alternative for some patients intolerant of the lenvatinib/everolimus combo. Future comparisons in more models are needed to assess and compare the efficacy and side-effect profiles of these two combinations.

Our findings demonstrate that the addition of sapanisertib to cabozantinib significantly reduces pERK levels compared with cabozantinib treatment alone. This suggests that sapanisertib acts synergistically with cabozantinib to restrain ERK phosphorylation, which seems to contribute to enhanced efficacy. Analysis of bulk RNA-seq data revealed that the combo treatment affects the activities of various ERK downstream TFs. ERK enhances downstream TF activities in two ways: (i) by phosphorylating FOS/JUN family members and MYC, thereby preventing their proteasomal degradation and increasing their DNA-binding activity (80); (ii) by phosphorylating and activating ternary complex factors that induce the transcription of immediate early genes (IEG), including JUN, FOS, MYC, and EGR families, which encode TFs (80). None of these TFs exhibited differential expression between the combo-treated samples and controls, suggesting that the downregulation of their activities may primarily be mediated through their phosphorylation by ERK. Further investigation into the post-translational modifications and functional interactions of these TFs is needed to fully understand the mechanisms underlying their regulation in response to the combo treatment. In addition, future studies should explore the crosstalk between ERK and other signaling pathways to gain a comprehensive understanding of the molecular events associated with the combo treatment.

This study demonstrated that the cabozantinib plus sapanisertib combination offers improved therapeutic effectiveness, compared with either therapy alone as well as various single and combinational treatments using drugs against targets selected by omics analyses of RCCs. This combo is even effective in tumors with prior exposure to TKIs targeting VEGFRs. Taken together, our study has shown that the cabozantinib and sapanisertib combination has the potential to be used as a first-line treatment for selected patients with ccRCC and especially as a second-line treatment for patients who have failed other TKI and ICI.

Authors' Disclosures

M.C. Wendl reports grants from NIH during the conduct of the study. A. Gould reports grants from NIH during the conduct of the study. B.E. Welm reports grants from NIH during the conduct of the study, and the University of Utah may license the models described herein to for-profit companies, which may result in tangible property royalties to members of the Welm lab who developed the models. M. Koh reports other support from Kuda Therapeutics Inc. outside the submitted work. A.L. Welm reports grants from AbbVie, other support from Modulus Therapeutics, and personal fees from LGChem Life Sciences Innovation Center outside the submitted work; and University of Utah may license the models described herein to for-profit companies, which may result in tangible property royalties to members of the Welm labs who developed the models. F. Meric-Bernstam reports personal fees from AbbVie, Aduro BioTech Inc., Alkermes, AstraZeneca, Daiichi Sankyo Co. Ltd., Calibr (a division of Scripps Research), DebioPharm, Ecor1 Capital, eFFECTOR Therapeutics, F. Hoffman-La Roche Ltd., GT Apeiron, Genentech Inc., Harbinger Health, IBM Watson, Infinity Pharmaceuticals, Jackson Laboratory, Kolon Life Science, LegoChem Bio, Lengo Therapeutics, Menarini Group, OrigiMed, PACT Pharma, Parexel International, Pfizer Inc., Protai Bio Ltd, Samsung Bioepis, Seattle Genetics Inc., Tallac Therapeutics, Tyra Biosciences, Xencor, Zymeworks, Black Diamond, Biovica, Eisai, FogPharma, Immunomedics, Inflection Biosciences, Karyopharm Therapeutics, Loxo Oncology, Mersana Therapeutics, OnCusp Therapeutics, Puma Biotechnology Inc., Seattle Genetics, Sanofi, Silverback Therapeutics, Spectrum Pharmaceuticals, Theratechnologies, and Zentalis; grants from Aileron Therapeutics, Inc., AstraZeneca, Bayer Healthcare Pharmaceutical, Calithera Biosciences Inc., Curis Inc., CytomX Therapeutics Inc., Daiichi Sankyo Co. Ltd., Debiopharm International, eFFECTOR Therapeutics, Genentech Inc., Guardant Health Inc., Klus Pharma, Takeda Pharmaceutical, Novartis, Puma Biotechnology Inc., Taiho Pharmaceutical Co., and other support from European Organisation for Research and Treatment of Cancer (EORTC), European Society for Medical Oncology (ESMO), and Cholangiocarcinoma Foundation outside the submitted work. S. Li reports other support from Inotiv, Inc. outside the submitted work. C.X. Ma reports grants from government during the conduct of the study. L. Ding reports grants from NIH outside the submitted work; in addition, L. Ding has a patent for Novel combinational treatment for ccRCC pending. F. Chen reports grants from NIH during the conduct of the study; in addition, F. Chen has a patent for Novel combinational treatment for ccRCC pending. No disclosures were reported by the other authors.

Disclaimer

This publication is solely the responsibility of the authors and does not necessarily represent the official view of NCRR, PRR, or NIH.

Authors' Contributions

Y. Wu: Conceptualization, data curation, formal analysis, visualization, writing–original draft, project administration, writing–review and editing. **S. Chen:** Formal analysis, validation, visualization, writing–review and editing. **X. Yang:** Data curation, validation, methodology, writing–original draft. **K. Sato:** Data curation, validation, methodology, writing–original draft, writing–review and editing. **P. Lal:** Data curation, methodology, writing–original draft, writing–review and editing. **Y. Wang:** Resources, methodology, writing–original draft. **A.T. Shinkle:** Validation. **M.C. Wendl:** Writing–review and editing. **T.M. Primeau:** Resources. **Y. Zhao:** Validation. **A. Gould:** Data curation. **H. Sun:** Resources, data curation. **J.L. Mudd:** Resources. **J. Hoog:** Formal analysis. **R.J. Mashl:** Data curation. **M.A. Wyczalkowski:** Visualization. **C.-K. Mo:** Formal analysis, writing–review and editing. **R. Liu:** Formal analysis. **J.M. Herndon:** Resources. **S.R. Davies:** Funding acquisition. **D. Liu:** Resources. **X. Ding:** Resources. **Y.A. Evrard:** Resources. **B.E. Welm:** Resources, methodology. **D. Lum:** Resources, methodology. **M. Koh:** Methodology. **A.L. Welm:** Methodology. **J.H. Chuang:** Supervision, writing–review and editing. **J.A. Moscow:** Writing–review and editing. **F. Meric-Bernstam:** Writing–review and editing. **R. Govindan:** Writing–review and editing. **S. Li:** Methodology, writing–review and editing. **J. Hsieh:** Resources, methodology, writing–review and editing. **R.C. Fields:** Resources, methodology. **K.-H. Lim:** Writing–review and editing. **C.X. Ma:**

Methodology. **H. Zhang:** Resources. **L. Ding:** Conceptualization, resources, supervision, funding acquisition, writing–review and editing. **F. Chen:** Conceptualization, resources, supervision, funding acquisition, writing–review and editing.

Acknowledgments

The authors thank the Genome Technology Access Center of the McDonnell Genome Institute at Washington University School of Medicine for help with genomic analysis. The Center is partially supported by NCI Cancer Center Support Grant #P30 CA91842 to the Siteman Cancer Center from the National Center for Research Resources (NCRR), a component of the NIH and NIH Roadmap for Medical Research. L. Ding and F. Chen are partially supported by NIH grants R01CA260112, U01DK131380, U54AG075934, and U2CCA223303. K. Sato has received overseas research fellowships from the Japan Society for the Promotion of Science (JSPS) and the Uehara Memorial Foundation. A.L. Welm, and B.E. Welm are supported by NCI award U54CA224076. Research reported in this publication also utilized the Preclinical Research Shared Resource at Huntsman Cancer Institute at the University of Utah and was supported by the NCI award P30CA042014. Finally, we are grateful to the patients, families, and professionals who have contributed to this study.

The publication costs of this article were defrayed in part by the payment of publication fees. Therefore, and solely to indicate this fact, this article is hereby marked "advertisement" in accordance with 18 USC section 1734.

Note

Supplementary data for this article are available at Cancer Research Online (http://cancerres.aacrjournals.org/).

Received March 1, 2023; revised July 17, 2023; accepted September 25, 2023; published first September 27, 2023.

References

1. Hsieh JJ, Purdue MP, Signoretti S, Swanton C, Albiges L, Schmidinger M, et al. Renal cell carcinoma. Nat Rev Dis Primer. 2017;3:17009.
2. Singer EA, Gupta GN, Srinivasan R. Update on targeted therapies for clear cell renal cell carcinoma. Curr Opin Oncol 2011;23:283–9.
3. Bedke J, Albiges L, Capitanio U, Giles RH, Hora M, Lam TB, et al. The 2021 updated European association of urology guidelines on renal cell carcinoma: immune checkpoint inhibitor–based combination therapies for treatment-naive metastatic clear-cell renal cell carcinoma are standard of care. Eur Urol 2021;80: 393–7.
4. Rassy E, Flippot R, Albiges L. Tyrosine kinase inhibitors and immunotherapy combinations in renal cell carcinoma. Ther Adv Med Oncol 2020;12: 1758835920907504.
5. Motzer R, Alekseev B, Rha S-Y, Porta C, Eto M, Powles T, et al. Lenvatinib plus pembrolizumab or everolimus for advanced renal cell carcinoma. N Engl J Med 2021;384:1289–300.
6. Motzer RJ, Powles T, Burotto M, Escudier B, Bourlon MT, Shah AY, et al. Nivolumab plus cabozantinib versus sunitinib in first-line treatment for advanced renal cell carcinoma (CheckMate 9ER): long-term follow-up results from an open-label, randomised, phase 3 trial. Lancet Oncol 2022;23:888–98.
7. Choueiri TK, Escudier B, Powles T, Mainwaring PN, Rini BI, Donskov F, et al. Cabozantinib versus everolimus in advanced renal-cell carcinoma. N Engl J Med. 2015;373:1814–23.
8. Pennacchietti S, Michieli P, Galluzzo M, Mazzone M, Giordano S, Comoglio PM. Hypoxia promotes invasive growth by transcriptional activation of the met protooncogene. Cancer Cell 2003;3:347–61.
9. Rankin EB, Fuh KC, Castellini L, Viswanathan K, Finger EC, Diep AN, et al. Direct regulation of GAS6/AXL signaling by HIF promotes renal metastasis through SRC and MET. Proc Natl Acad Sci USA 2014;111:13373–8.
10. Gibney GT, Aziz SA, Camp RL, Conrad P, Schwartz BE, Chen CR, et al. c-Met is a prognostic marker and potential therapeutic target in clear cell renal cell carcinoma. Ann Oncol 2013;24:343–9.
11. Choueiri TK, Escudier B, Powles T, Tannir NM, Mainwaring PN, Rini BI, et al. Cabozantinib versus everolimus in advanced renal cell carcinoma (METEOR): final results from a randomised, open-label, phase 3 trial. Lancet Oncol 2016;17: 917–27.
12. Choueiri TK, Halabi S, Sanford BL, Hahn O, Michaelson MD, Walsh MK, et al. Cabozantinib versus sunitinib as initial targeted therapy for patients with metastatic renal cell carcinoma of poor or intermediate risk: the alliance A031203 CABOSUN trial. J Clin Oncol. 2017;35:591–7.
13. Hsieh AC, Liu Y, Edlind MP, Ingolia NT, Janes MR, Sher A, et al. The translational landscape of mTOR signalling steers cancer initiation and metastasis. Nature 2012;485:55–61.
14. García-García C, Ibrahim YH, Serra V, Calvo MT, Guzmán M, Grueso J, et al. Dual mTORC1/2 and HER2 blockade results in antitumor activity in preclinical models of breast cancer resistant to anti-HER2 therapy. Clin Cancer Res 2012;18: 2603–12.
15. Hua H, Kong Q, Zhang H, Wang J, Luo T, Jiang Y. Targeting mTOR for cancer therapy. J Hematol OncolJ Hematol Oncol 2019;12:71.
16. Voss MH, Gordon MS, Mita M, Rini B, Makker V, Macarulla T, et al. Phase 1 study of mTORC1/2 inhibitor sapanisertib (TAK-228) in advanced solid tumours, with an expansion phase in renal, endometrial or bladder cancer. Br J Cancer 2020;123:1590–8.
17. Paik PK, Ahn LSH, Plodkowski AJ, Fan P-D, Rudin CM. Phase II study of TAK228 in patients with advanced non-small cell lung cancer (NSCLC) harboring NFE2L2 and KEAP1 mutations. J Clin Oncol. 2020;38:9607.
18. McGregor BA, Xie W, Adib E, Stadler WM, Zakharia Y, Alva A, et al. Biomarker-based phase II study of sapanisertib (TAK-228): an mTORC1/2 inhibitor in patients with refractory metastatic renal cell carcinoma. JCO Precis Oncol 2022; 6:e2100448.
19. Shang R, Song X, Wang P, Zhou Y, Lu X, Wang J, et al. Cabozantinib-based combination therapy for the treatment of hepatocellular carcinoma. Gut 2021; 70:1746–57.
20. Hsieh JJ, Le VH, Oyama T, Ricketts CJ, Ho TH, Cheng EH. Chromosome 3p loss–orchestrated VHL, HIF, and epigenetic deregulation in clear cell renal cell carcinoma. J Clin Oncol 2018;36:3533–9.
21. Small J, Washburn E, Millington K, Zhu J, Holder SL. The addition of abemaciclib to sunitinib induces regression of renal cell carcinoma xenograft tumors. Oncotarget 2017;8:95116–34.
22. Zou Y, Wang J, Leng X, Huang J, Xue W, Zhang J, et al. The selective MEK1 inhibitor Selumetinib enhances the antitumor activity of everolimus against renal cell carcinoma in vitro and in vivo. Oncotarget 2017;8:20825–33.
23. Patnaik A, Rosen LS, Tolaney SM, Tolcher AW, Goldman JW, Gandhi L, et al. Efficacy and safety of abemaciclib, an inhibitor of CDK4 and CDK6, for patients with breast cancer, non-small cell lung cancer, and other solid tumors. Cancer Discov 2016;6:740–53.
24. Noonan AM, Bunch KP, Chen J-Q, Herrmann MA, Lee J, Kohn EC, et al. Pharmacodynamic markers and clinical results from the phase II study of the SMAC-Mimetic birinapant in women with relapsed platinum-resistant or refractory epithelial ovarian cancer. Cancer 2016;122:588–97.
25. Lee K, Zhang H, Qian DZ, Rey S, Liu JO, Semenza GL. Acriflavine inhibits HIF-1 dimerization, tumor growth, and vascularization. Proc Natl Acad Sci USA 2009; 106:17910–5.
26. Mangraviti A, Raghavan T, Volpin F, Skuli N, Gullotti D, Zhou J, et al. HIF-1α-targeting acriflavine provides long term survival and radiological tumor response in brain cancer therapy. Sci Rep 2017;7:14978.
27. Nargund AM, Pham CG, Dong Y, Wang PI, Osmangeyoglu HU, Xie Y, et al. The SWI/SNF protein PBRM1 restrains VHL-loss-driven clear cell renal cell carcinoma. Cell Rep 2017;18:2893–906.
28. Juengel E, Nowaz S, Makarevi J, Natsheh I, Werner I, Nelson K, et al. HDAC-inhibition counteracts everolimus resistance in renal cell carcinoma in vitro by diminishing cdk2 and cyclin A. Mol Cancer 2014;13:152.
29. Pinter M, Jain RK. Targeting the renin-angiotensin system to improve cancer treatment: Implications for immunotherapy. Sci Transl Med 2017;9:eaan5616.
30. Cui Zhou D, Jayasinghe RG, Chen S, Herndon JM, Iglesia MD, Navale P, et al. Spatially restricted drivers and transitional cell populations cooperate with the microenvironment in untreated and chemo-resistant pancreatic cancer. Nat Genet 2022;54:1390–405.
31. Sun H, Cao S, Mashl RJ, Mo C-K, Zaccaria S, Wendl MC, et al. Comprehensive characterization of 536 patient-derived xenograft models prioritizes candidates for targeted treatment. Nat Commun 2021;12:5086.

32. Ahdesmäki MJ, Gray SR, Johnson JH, Lai Z. Disambiguate: an open-source application for disambiguating two species in next generation sequencing data from grafted samples. F1000Res 2017;5:2741.
33. Kim S, Scheffler K, Halpern AL, Bekritsky MA, Noh E, Källberg M, et al. Strelka2: fast and accurate calling of germline and somatic variants. Nat Methods 2018;15:591–4.
34. Cibulskis K, Lawrence MS, Carter SL, Sivachenko A, Jaffe D, Sougnez C, et al. Sensitive detection of somatic point mutations in impure and heterogeneous cancer samples. Nat Biotechnol 2013;31:213–9.
35. Koboldt DC, Zhang Q, Larson DE, Shen D, McLellan MD, Lin L, et al. VarScan 2: Somatic mutation and copy number alteration discovery in cancer by exome sequencing. Genome Res 2012;22:568–76.
36. Ye K, Schulz MH, Long Q, Apweiler R, Ning Z. Pindel: a pattern growth approach to detect break points of large deletions and medium sized insertions from paired-end short reads. Bioinforma Oxf Engl 2009;25:2865–71.
37. Bray NL, Pimentel H, Melsted P, Pachter L. Near-optimal probabilistic RNA-seq quantification. Nat Biotechnol 2016;34:525–7.
38. Soneson C, Love MI, Robinson MD. Differential analyses for RNA-seq: transcript-level estimates improve gene-level inferences. F1000Research 2015;4:1521.
39. Li Y, Lih T-SM, Dhanasekaran SM, Mannan R, Chen L, Cieslik M, et al. Histopathologic and proteogenomic heterogeneity reveals features of clear cell renal cell carcinoma aggressiveness. Cancer Cell 2023;41:139–63.
40. Callister SJ, Barry RC, Adkins JN, Johnson ET, Qian W-J, Webb-Robertson B-JM, et al. Normalization approaches for removing systematic biases associated with mass spectrometry and label-free proteomics. J Proteome Res 2006;5:277–86.
41. Bolstad B. preprocessCore: A collection of pre-processing functions [Internet]. Bioconductor version: Release (3.15); 2022. Available from: https://bioconductor.org/packages/preprocessCore/.
42. Clark DJ, Dhanasekaran SM, Petralia F, Pan J, Song X, Hu Y, et al. Integrated proteogenomic characterization of clear cell renal cell carcinoma. Cell 2019;179:964–83.
43. Liberzon A, Birger C, Thorvaldsdóttir H, Ghandi M, Mesirov JP, Tamayo P. The Molecular Signatures Database (MSigDB) hallmark gene set collection. Cell Syst 2015;1:417–25.
44. Yu G, Wang L-G, Han Y, He Q-Y. clusterProfiler: an R package for comparing biological themes among gene clusters. Omics J Integr Biol 2012;16:284–7.
45. Wu Y, Terekhanova NV, Caravan W, Naser Al Deen N, Lal P, Chen S, et al. Epigenetic and transcriptomic characterization reveals progression markers and essential pathways in clear cell renal cell carcinoma. Nat Commun 2023;14:1681.
46. Stuart T, Butler A, Hoffman P, Hafemeister C, Papalexi E, Mauck WM, et al. Comprehensive integration of single-cell data. Cell 2019;177:1888–902.
47. Blondel VD, Guillaume J-L, Lambiotte R, Lefebvre E. Fast unfolding of communities in large networks. J Stat Mech Theory Exp 2008;2008:P10008.
48. Posadas EM, Limvorasak S, Figlin RA. Targeted therapies for renal cell carcinoma. Nat Rev Nephrol 2017;13:496–511.
49. Kotecha RR, Motzer RJ, Voss MH. Towards individualized therapy for metastatic renal cell carcinoma. Nat Rev Clin Oncol 2019;16:621–33.
50. Smith SF, Collins SE, Charest PG. Ras, PI3K and mTORC2 - three's a crowd? J Cell Sci 2020;133:jcs234930.
51. Nisa L, Häfliger P, Poliaková M, Giger R, Francica P, Aebersold DM, et al. PIK3CA hotspot mutations differentially impact responses to MET targeting in MET-driven and non-driven preclinical cancer models. Mol Cancer 2017;16:93.
52. Janku F, Hong DS, Fu S, Piha-Paul SA, Naing A, Falchook GS, et al. Assessing PIK3CA and PTEN in early-phase trials with PI3K/AKT/mTOR inhibitors. Cell Rep 2014;6:377–87.
53. Yakes FM, Chen J, Tan J, Yamaguchi K, Shi Y, Yu P, et al. Cabozantinib (XL184), a novel MET and VEGFR2 inhibitor, simultaneously suppresses metastasis, angiogenesis, and tumor growth. Mol Cancer Ther 2011;10:2298–308.
54. Vitkevičienė A, Janulis V, Žučenka A, Borutinskaitė V, Kaupinis A, Valius M, et al. Oxidative phosphorylation inhibition induces anticancerous changes in therapy-resistant-acute myeloid leukemia patient cells. Mol Carcinog 2019;58:2008–16.
55. Du B, Shim JS. Targeting epithelial-mesenchymal transition (EMT) to overcome drug resistance in cancer. Mol Basel Switz 2016;21:E965.
56. Shibue T, Weinberg RA. EMT, CSCs, and drug resistance: the mechanistic link and clinical implications. Nat Rev Clin Oncol 2017;14:611–29.
57. Abdelaziz A, Vaishampayan U. Cabozantinib for the treatment of kidney cancer. Expert Rev Anticancer Ther 2017;17:577–84.
58. Siska PJ, Beckermann KE, Rathmell WK, Haake SM. Strategies to overcome therapeutic resistance in renal cell carcinoma. Urol Oncol 2017;35:102–10.
59. Guo H, German P, Bai S, Barnes S, Guo W, Qi X, et al. The PI3K/AKT pathway and renal cell carcinoma. J Genet Genomics Yi Chuan Xue Bao 2015;42:343–53.
60. Samuels Y, Wang Z, Bardelli A, Silliman N, Ptak J, Szabo S, et al. High frequency of mutations of the PIK3CA gene in human cancers. Science 2004;304:554.
61. Samuels Y, Diaz LA, Schmidt-Kittler O, Cummins JM, Delong L, Cheong I, et al. Mutant PIK3CA promotes cell growth and invasion of human cancer cells. Cancer Cell 2005;7:561–73.
62. Bell JL, Wächter K, Mühleck B, Pazaitis N, Köhn M, Lederer M, et al. Insulin-like growth factor 2 mRNA-binding proteins (IGF2BPs): post-transcriptional drivers of cancer progression? Cell Mol Life Sci CMLS 2013;70:2657–75.
63. Lederer M, Bley N, Schleifer C, Hüttelmaier S. The role of the oncofetal IGF2 mRNA-binding protein 3 (IGF2BP3) in cancer. Semin Cancer Biol 2014;29:3–12.
64. Xu W, Sheng Y, Guo Y, Huang Z, Huang Y, Wen D, et al. Increased IGF2BP3 expression promotes the aggressive phenotypes of colorectal cancer cells in vitro and vivo. J Cell Physiol 2019;234:18466–79.
65. Pei X, Li M, Zhan J, Yu Y, Wei X, Guan L, et al. Enhanced IMP3 expression activates NF-8B pathway and promotes renal cell carcinoma progression. PLoS One 2015;10:e0124338.
66. Tschirdewahn S, Panic A, Püllen L, Harke NN, Hadaschik B, Riesz P, et al. Circulating and tissue IMP3 levels are correlated with poor survival in renal cell carcinoma. Int J Cancer 2019;145:531–9.
67. Hoffmann NE, Sheinin Y, Lohse CM, Parker AS, Leibovich BC, Jiang Z, et al. External validation of IMP3 expression as an independent prognostic marker for metastatic progression and death for patients with clear cell renal cell carcinoma. Cancer 2008;112:1471–9.
68. Jiang Z, Chu PG, Woda BA, Rock KL, Liu Q, Hsieh C-C, et al. Analysis of RNA-binding protein IMP3 to predict metastasis and prognosis of renal-cell carcinoma: a retrospective study. Lancet Oncol 2006;7:556–64.
69. Mancarella C, Scotlandi K. IGF2BP3 from physiology to cancer: novel discoveries, unsolved issues, and future perspectives. Front Cell Dev Biol 2020;7:363.
70. Kuo C-L, Chou H-Y, Chiu Y-C, Cheng AN, Fan C-C, Chang Y-N, et al. Mitochondrial oxidative stress by Lon-PYCR1 maintains an immunosuppressive tumor microenvironment that promotes cancer progression and metastasis. Cancer Lett 2020;474:138–50.
71. Hu F, Zeng W, Liu X. A gene signature of survival prediction for kidney renal cell carcinoma by multi-omic data analysis. Int J Mol Sci 2019;20:E5720.
72. Wu Y, Zhang X, Wei X, Feng H, Hu B, Deng Z, et al. A mitochondrial dysfunction and oxidative stress pathway-based prognostic signature for clear cell renal cell carcinoma. Oxid Med Cell Longev 2021;2021:e9939331.
73. Zhou L, Liu X-D, Sun M, Zhang X, German P, Bai S, et al. Targeting MET and AXL overcomes resistance to sunitinib therapy in renal cell carcinoma. Oncogene 2016;35:2687–97.
74. Ciamporcero E, Miles KM, Adelaiye R, Ramakrishnan S, Shen L, Ku SY, et al. Combination strategy targeting VEGF and HGF/c-met in human renal cell carcinoma models. Mol Cancer Ther 2015;14:101–10.
75. Tolaney SM, Ziehr DR, Guo H, Ng MR, Barry WT, Higgins MJ, et al. Phase II and biomarker study of cabozantinib in metastatic triple-negative breast cancer patients. Oncologist 2017;22:25–32.
76. Goyal L, Zheng H, Yurgelun MB, Abrams TA, Allen JN, Cleary JM, et al. A phase II and biomarker study of cabozantinib in patients with advanced cholangiocarcinoma. Cancer 2017;123:1979–88.
77. Powles T, Choueiri TK, Motzer RJ, Jonasch E, Pal S, Tannir NM, et al. Outcomes based on plasma biomarkers in METEOR, a randomized phase 3 trial of cabozantinib vs everolimus in advanced renal cell carcinoma. BMC Cancer 2021;21:904.
78. Rimassa L, Kelley RK, Meyer T, Ryoo B-Y, Merle P, Park J-W, et al. Outcomes based on plasma biomarkers for the phase 3 CELESTIAL trial of cabozantinib versus placebo in advanced hepatocellular carcinoma. Liver Cancer 2022;11:38–47.
79. Schmidinger M, Danesi R. Management of adverse events associated with cabozantinib therapy in renal cell carcinoma. Oncologist 2018;23:306–15.
80. Lavoie H, Gagnon J, Therrien M. ERK signalling: a master regulator of cell behaviour, life and fate. Nat Rev Mol Cell Biol 2020;21:607–32.